Old Dominion University
ODU Digital Commons

OES Theses and Dissertations
Ocean & Earth Sciences

Summer 2019

The Evolution of the El Niño-Southern Oscillation and Tropical Pacific Climate Across the Last Deglaciation

Ryan Hunter Glaubke
Old Dominion University, rglaubke@marine.rutgers.edu

Follow this and additional works at: https://digitalcommons.odu.edu/oeas_etds

Part of the Climate Commons, and the Geochemistry Commons

Recommended Citation

Glaubke, Ryan H.. "The Evolution of the El Niño-Southern Oscillation and Tropical Pacific Climate Across the Last Deglaciation" (2019). Master of Science (MS), Thesis, Ocean & Earth Sciences, Old Dominion University, DOI: 10.25777/mk6r-kg66
https://digitalcommons.odu.edu/oeas_etds/171

This Thesis is brought to you for free and open access by the Ocean & Earth Sciences at ODU Digital Commons. It has been accepted for inclusion in OES Theses and Dissertations by an authorized administrator of ODU Digital Commons. For more information, please contact digitalcommons@odu.edu.

THE EVOLUTION OF THE EL NIÑO – SOUTHERN OSCILLATION AND TROPICAL PACIFIC CLIMATE ACROSS THE LAST DEGLACIATION

by

Ryan Hunter Glaubke
B.S. May 2016, Old Dominion University

A Thesis Submitted to the Faculty of Old Dominion University in
Partial Fulfillment of the Requirements for the Degree of

MASTER OF SCIENCE

OCEAN AND EARTH SCIENCES

OLD DOMINION UNIVERSITY
August 2019

Approved by:

Matthew W. Schmidt (Director)

David J. Burdige (Member)

Richard C. Zimmerman (Member)

ABSTRACT

THE EVOLUTION OF THE EL NIÑO – SOUTHERN OSCILLATION AND TROPICAL PACIFIC CLIMATE ACROSS THE LAST DEGLACIATION

Ryan Hunter Glaubke
Old Dominion University, 2019
Director: Dr. Matthew W. Schmidt

The El Niño – Southern Oscillation (ENSO) is the largest interannual component of Earth's climate system, capable of exerting significant influence over global climate patterns that affect communities around the globe. Nevertheless, a comprehensive understanding of the ENSO system and its relationship to tropical Pacific climate dynamics remains unclear. Although new paleoceanographic proxies have shown promise in in their ability to constrain past ENSO change, little is known about how ENSO varied in response to millennial-scale climate events over the last 25,000 years. Here, I present new records of tropical Pacific mean state and ENSO variability over the last 25,000 years reconstructed from a high-resolution sediment core recovered from the Eastern Equatorial Pacific (EEP) cold tongue (MV1014-02-17JC, 0°10.8′ S, 85°52.0′ W, 2846 m water depth). Mean state changes are reconstructed by measuring Mg/Ca ratios in the thermocline-dwelling foraminifera *Neogloboquadrina dutertrei*. In addition, I performed Individual Foraminiferal Analysis (IFA) on single *N. dutertrei* shells from seven targeted time slices in order to estimate thermocline temperature variability under different climate regimes across the last deglaciation. I combine these results with Monte Carlo simulations of hypothetical ENSO change and robust, nonparametric statistics to reconstruct "snapshots" of past ENSO activity from the Holocene, the Last Glacial Maximum (LGM), and the abrupt climate events of the last deglaciation. Taken together, the results indicate that Modern/Late Holocene ENSO activity is more variable than at any other time in the last 25,000 years. I speculate that a combination of orbital forcing, changes in upper ocean thermal stratification, trade wind strength, and the mean position of the Intertropical Convergence Zone (ITCZ) acted to suppress past ENSO variability. These results emphasize the dynamic relationship between tropical Pacific climate and the ENSO and underscore the need for more detailed studies under variable background conditions in order to predict future ENSO evolution in an anthropogenically warming world.

Copyright, 2019, by Ryan Hunter Glaubke, All Rights Reserved

This thesis is dedicated to Marjorie Fay Glaubke.
You shed more light on this world than I ever could.

ACKNOWLDGEMENTS

As scientists, the search for truth and the generation of new knowledge can be a trying and arduous responsibility. This is multiplied exponentially for a graduate student trying it for the very first time. Indeed, without the guidance, instruction, and unwavering support of my colleagues, friends, and family, the completion of this thesis manuscript would never have been possible. I am forever indebted to them.

First and foremost, I would like to acknowledge my deepest appreciation for my primary advisor, Dr. Matthew Schmidt. Matthew's encouraging demeanor, knowledgeable instruction, and limitless patience kept me motivated at times when I needed it most. I am proud to have been able to work beneath a scientist whose keen sense of curiosity is only outdone by his radiant kindness. I am also grateful to Dr. Jennifer Hertzberg—my de facto second advisor—for keeping me sane, entertaining my wide-eyed and hand-waving theories, and demonstrating to me first-hand what it means to truly love what you do. The remaining members of the Schmidt Lab have each helped immensely to bring this project to life: a huge thanks to Lenzie Ward, for spending hours under the microscope to get this project off of the ground; to my lab mates Brian Close and Colton Watkins, for never letting me take the job too seriously; and to Bettina Sohst, for her unmatched talent and patience on the ICP-MS. A thank you is also in order for my committee members, Drs. David Burdige and Richard Zimmerman, for always having time to chat about ideas and ways to make this project the best it could truly be.

The ENSO is a notoriously complicated climate phenomenon, and so the ideas presented in this manuscript benefitted greatly from multiple discussions with colleagues on the forefront of paleo-ENSO and tropical Pacific paleoclimate research. I would like to thank Dr. Heather

Ford of Queen Mary University of London and Sarah White of the University of California, Santa Cruz for conversations surrounding model development. I also thank Dr. Pratigya Polissar at the Lamont-Doherty Earth Observatory at Columbia University and Dr. Kris Karnauskas at the University of Colorado, Boulder for their consultation on data interpretation.

More importantly, however, I would never have come as far as I have without the love and support of my friends and family. At times when the burden of graduate school weighed heaviest, or when I would think myself into a corner and get frustrated, or when we would have to completely restart data collection due to some minor contamination problems (four separate times), I never had to turn far for a warm smile, an encouraging word, and an assurance that the work I was doing was good. To my friends: thank you, especially to my friends in the graduate program: DuPree Ashburn, Ali Burgos, Shannon Cofield, Svienn Einnarson, Maddie Hummel, Praveen Kumar, Alfonso Macías, Rachel McMahon, Kyle McQuiggan, Corday Selden, Bryce Shoup, and Lauren Sommers. To my Dad and my little sister, Madison: I love you, and thank you for always loving and believing in me. And finally, to my Mom: I love you, I miss you, and I wish you could be here to celebrate this milestone with me. This thesis is dedicated to you.

NOMENCLATURE

AMOC	Atlantic Meridional Overturning Circulation
BA	Bølling-Allerød
BSD	Biweight Standard Deviation
COSMIC	College of Sciences Mass Instrumentation Cluster
ECDF	Empirical Cumulative Distribution Function
EEP	Eastern Equatorial Pacific
EH	Early Holocene
ENSO	El Niño – Southern Oscillation
EUC	Equatorial Undercurrent
HR-ICP-MS	High Resolution Inductively Coupled Plasma Mass Spectrometer
HS1	Heinrich Stadial 1
IFA	Individual Foraminiferal Analysis
INFAUNAL	Individual Foraminiferal Approach Uncertainty Analysis
IR-MS	Isotope Ratio Mass Spectrometer
ITCZ	Intertropical Convergence Zone
Kyr	Kiloyear, 1000 years
LGM	Last Glacial Maximum
MH	Mid-Holocene
MIS	Marine Isotope Stage
Modern/LH	Modern/Late Holocene
NGRIP	North Greenland Ice Core Project

NOMENCLATURE (CONT.)

NOAA	National Oceanic and Atmospheric Administration
NOSAMS	National Ocean Sciences Accelerator Mass Spectrometry
PSU	Paleo-Seawater Uncertainty
Q-Q	Quantile-Quantile
SST	Sea Surface Temperature
TAO	Tropical Atmosphere Ocean Array
VPDB	Vienna Pee Dee Belemnite Standard
YD	Younger Dryas

TABLE OF CONTENTS

Page

LIST OF TABLES x

LIST OF FIGURES xi

1. INTRODUCTION 1

2. REGIONAL SETTING 8
    2.1 OCEANOGRAPHY OF THE EASTERN EQUATORIAL PACIFIC 8
    2.2 *NEOGLOBOQUADRINA DUTERTREI* AS A RECORDER OF SUBSURFACE TEMPERATURE VARIABILITY 11

3. MATERIALS AND METHODS 13
    3.1 ANALYTICAL TECHNIQUES 13
        3.1.1 AGE MODEL DEVELOPMENT 13
        3.1.2 MULTI-SHELL MINOR AND TRACE ELEMENT ANALYSES 14
        3.1.3 INDIVIDUAL FORAMINIFERAL ANALYSIS 15
        3.1.4 CALCULATING SUBSURFACE TEMPERATURES 17
        3.1.5 STABLE ISOTOPE ANALYSIS AND CALCULATING ICE VOLUME FREE-$\delta^{18}O_{SW}$ 18
    3.2 STATISTICAL APPROACH 20
    3.3 BOOTSTRAP SENSITIVITY ANALYSIS 23

4. RESULTS 25
    4.1 SUBSURFACE TEMPERATURE AND SALINITY RECORDS 25
    4.2 SENSITIVITY MODEL RESULTS 26
    4.3 BIWEIGHT ESTIMATES OF INDIVIDUAL FORAMINIFERA DATA 29
    4.4 QUANTILE-QUANTILE ANALYSES 30

5. DISCUSSION 32
    5.1 IMPLICATIONS OF STATISTICAL TREATMENT ON ENSO INTERPRETATION 32
    5.2 THE HOLOCENE 34
    5.3 THE LAST GLACIAL MAXIMUM 39
    5.4 THE LAST DEGLACIATION 45

6. CONCLUSIONS 50

REFERENCES 52

FIGURES AND TABLES 66

VITA 85

LIST OF TABLES

Table Page

1. Time horizons targeted for Individual Foraminiferal Analysis 71

2. Monte Carlo Average BSDs and Associated Confidence Limits 73

3. Results from the two-sample Kolmogorov-Smirnov Goodness-of-Fit Tests 77

4. Results from the Brown-Forsythe Tests for Homogeneity of Variance 78

LIST OF FIGURES

Figure Page

1. Regional map of the eastern equatorial Pacific 66

2. Modern hydrographic data illustrating the different modes of surface and subsurface temperature variability within the EEP 68

3. The age model for sediment core 17JC 69

4. Linear regressions of Mg/Ca against cleaning indicators and sample size for bulk and IFA geochemical data....................70

5. Down-core records of Mg/Ca-derived subsurface temperature and IVF-$\delta^{18}O_{SW}$ plotted with the NGRIP $\delta^{18}O$ ice core record of Greenland air temperature 72

6. Comparison of BSD uncertainty estimates from the 50% dampened ENSO scenario and the 60% amplified ENSO scenario against the non-adjusted ENSO scenario 74

7. Bar graphs summarizing the sensitivity of the warmest three quantiles to prescribed changes in the amplitude of ENSO 75

8. IFA data and related distributions from seven discrete time slices spanning the last 25 kyrs 76

9. Q-Q plot comparing the quantiles of the TAO temperature observations at 40 m against the quantiles from the Modern/LH population of individual foraminifera from the 09MC core-top 79

10. Q-Q plots comparing the quantiles from the 17JC down-core Holocene time slices against the Mod/LH population of individual foraminifera 80

11. Q-Q plots comparing the quantiles from the 17JC down-core deglacial and LGM time slices against the Mod/LH population of individual foraminifera 81

12. Comparison of two independently generated paleotemperature distributions from the core-top of 09MC 82

13. A synthesis of geochemical proxy records illustrating tropical Pacific mean state change over the last 25 kyrs 84

1. Introduction

In recent years, a fundamental uncertainty surrounding the connection between the El Niño – Southern Oscillation (ENSO) and Earth's warming climate over the last century has motivated investigations into the paleoceanographic history of the equatorial Pacific. In particular, efforts have been directed at understanding the environmental forcings and mechanisms that underpin the modulation of past ENSO activity. As the largest mode of interannual variability in Earth's climate system (Wang and Fiedler, 2006), the modern-day ENSO exerts a significant influence over global weather patterns, bioeconomies (particularly fisheries), the outbreak of certain diseases, and the success or failure of agriculture worldwide (Haines et al., 2006 and references therein). ENSO dynamics also have a profound effect on global average temperatures, as evidenced in 2016 when the record-breaking 2015/16 El Niño event helped boost global surface temperatures to their warmest in the instrumental record (Blunden et al., 2018). In spite of its importance for civil adaptation in the face of anthropogenic climate change, a comprehensive understanding of the ENSO system and its relationship to tropical Pacific climate dynamics remains unclear. Although coupled ocean-atmosphere climate model simulations of future emissions scenarios generally agree on the broader climatological response of the tropical Pacific to anthropogenic warming (Cai et al., 2015), substantial uncertainty remains in the future of ENSO, with model outputs in disagreement over the magnitude and sign of potential ENSO change (Latif and Keenlyside, 2009; Collins et al., 2010; Rashid et al., 2016). Such discrepancies in model projections can be remedied, however, with insights obtained from paleoenvironmental archives of past ENSO variability. Proxy records have the potential to evaluate the range of ENSO variability under different background climate states. In particular, a better understanding of how ENSO evolved across periods of abrupt climate change could help constrain the range of future ENSO variability in an anthropogenically warming world.

Although paleoclimate and modeling studies investigating paleo-ENSO across a broad range of timescales have been undertaken in the last several decades, a consensus regarding past ENSO variability and its relationship to tropical Pacific mean state remains elusive (see Lu et al., 2018 for a more comprehensive review). Proxy records of paleo-ENSO have been sought and extracted from numerous paleoenvironmental archives including deep sea sediments (Koutavas et al., 2002, 2006; Pena et al., 2008; Leduc et al., 2009b; Khider et al., 2011; Koutavas and Joanides, 2012; Sadekov et al., 2013; Ford et al., 2015; Rustic et al., 2015; White et al., 2017), fossil corals (Tudhope et al., 2001; Cobb et al., 2003; Woodroffe et al., 2003; McGregor and Gagan, 2004; Emile-Geay et al., 2016), and lake sediments (Rodbell et al., 1999; Moy et al., 2002; Conroy et al., 2008), yet the patterns of ENSO activity exhibited among these records are often difficult to reconcile. As a consequence, there is disagreement over the relative importance of dynamic feedback processes responsible for modulating ENSO.

A collection of studies investigating glacial-interglacial differences in ENSO activity make arguments in support of both enhanced (Koutavas et al., 2002, 2006; Koutavas and Joanides, 2012; Sadekov et al., 2013) and diminished ENSO variability (Ford et al., 2015; Leduc et al., 2009b) during the Last Glacial Maximum (LGM; 19 to 25 kyrs) relative to the Holocene. Studies which suggest an enhanced LGM ENSO observe an inverse relationship between the tropical Pacific zonal sea surface temperature (SST) gradient and ENSO variability, suggesting that tropical Pacific surface hydrography plays an important role in regulating ENSO (Koutavas and Joanides, 2012; Sadekov et al., 2013). The mechanism, known as the “ocean dynamical thermostat” (Clement et al., 1996), assumes a stationary dynamic coupling between zonal temperature patterns in the tropical Pacific and trade wind strength, where ENSO amplitude is modulated by changes in the zonal SST gradient in response to Earth's precession cycle (Clement et al., 2000). In contrast, other paleo-ENSO reconstructions find a reduction in ENSO activity during the LGM (Ford et al., 2015; Leduc et al., 2009b). These studies argue for a more dynamic relationship between ENSO and tropical Pacific climate, where the relative strength of individual feedbacks that govern ENSO behavior are highly dependent upon background climate conditions (Ford et al., 2015; Merkel et al., 2010; Bush, 2007). In addition, modeling studies are similarly inconsistent on estimates of LGM ENSO variability (Zheng et al., 2008), simulating both enhanced (An et al., 2004; Merkel et al., 2010; Otto-Bliesner et al., 2003) and diminished amplitude (Otto-Bliesner et al., 2006a; Bush, 2007; Zhu et al., 2017).

Studies investigating ENSO variability across the Holocene (the last 10 thousand years (kyrs)) are slightly less controversial. A growing body of marine sediment, coral, and lake records have converged around some generalized patterns of Holocene ENSO activity, most notably a reduction in ENSO variability during the early to mid-Holocene (Rodbell et al., 1999; Tudhope et al., 2001; Moy et al., 2002; McGregor and Gagan; 2004; Koutavas et al., 2006; Conroy et al., 2008; Koutavas and Joanides, 2012; Chen et al., 2016; Emile-Geay et al., 2016; White et al., 2017). These findings are supported by a suite of climate model simulations (Bush, 2007; Emile-Geay et al., 2007; Zheng et al., 2008; Brown et al., 2008; Braconnot et al., 2012; An and Choi, 2014; Liu et al., 2014) which consistently reproduce diminished ENSO variability during the early to mid-Holocene relative to the present. Both proxy records and model simulations have identified Earth's precession cycle as the primary modulator of ENSO activity across this period, although the exact feedback mechanisms which dampen ENSO are a matter of ongoing debate (Lu et al., 2018). In spite of this general data-model agreement, some proxy records find no significant ENSO reduction across the Holocene (Cobb et al., 2003; Leduc et al., 2009b) and some even show an enhanced ENSO (Corrège et al., 2000). The debate persists even over the last millennium, where high resolution marine records suggest both a varying (Rustic et al., 2015) and unvarying ENSO (Khider et al., 2011) in response to changing background conditions associated with the Medieval Climate Anomaly and the Little Ice Age.

In contrast to the Holocene and LGM, ENSO variability during the last deglaciation (approximately the last 10 – 20 kyrs) is considerably less constrained due to the paucity of high-resolution records spanning this interval of Earth's climate history (Lu et al., 2018). The period of transition between the LGM and the Holocene was one of abrupt climate change, characterized by pulses of increasing greenhouse gas concentrations (Petit et al., 1999; Bereiter et al., 2015), retreating ice sheets (Carlson et al., 2008; Bentley et al., 2010), rising sea levels (Fairbanks, 1989; Lambeck et al., 2014), and sweeping reorganizations of ocean and atmospheric circulation (McManus et al., 2004; Schmidt et al., 2012b; Koutavas and Lynch-Stieglitz, 2004; Broccoli et al., 2006). These major changes in climate boundary conditions were the result of large millennial-scale climate oscillations that toggled the planet's climate system between warmer interstadial periods (the Bølling – Allerød) and colder stadial periods (the Younger Dryas and Heinrich Stadial 1). Theoretically, these oscillations in global climate would substantially alter the coupled ocean-atmosphere system in the tropical Pacific, and by extension ENSO variability. Despite this, only a few studies have investigated paleo-ENSO intensity during the deglacial period (Sadekov et al., 2013; Koutavas and Joanides, 2012; White et al., 2017). The data currently available are either too sparse to draw broader inferences of ENSO behavior during periods of abrupt climate change (Leduc et al., 2009b; White et al., 2017) or sampling resolution constraints preclude the ability to tie estimates of ENSO variability to any particular climate event (Sadekov et al., 2013).

The difficulty in generating reliable records of paleo-ENSO from the deglacial period lies primarily in the limits of coral and marine sediment archives. Coral skeletons from ENSO-sensitive regions have traditionally been the gold standard for paleo-ENSO reconstructions due to their robust age model constraints (U-Th series dating) and seasonally-resolved bands (Tudhope et al., 2001; Cobb et al., 2003). Nevertheless, coral records generally only provide limited and discontinuous temporal coverage (restricted to centuries), complicating their use for long-term investigations of paleo-ENSO. In this respect, marine sediment archives can be useful for examining ENSO behavior on longer timescales and over a greater range of possible climate regimes. However, limitations such as low sedimentation rates (i.e. coarse time resolution) have made it difficult to extract high-frequency climate signals from marine sediment which often encompass centuries of time within single stratigraphic intervals.

This problem can be overcome by recent advances in trace element analytical techniques, notably the increased precision in the measurement of trace element ratios in single foraminiferal tests (Marchitto et al., 2006). These advances have led to the development of novel methods for reconstructing high-frequency hydrographic variability from marine sediments (Wit et al., 2010; Sadekov et al., 2013; Ford et al., 2015; White et al., 2017; Schmitt et al., 2019). One such example, Individual Foraminiferal Analysis (IFA), relies on inferences drawn from the descriptive statistics of geochemical parameters derived from populations of individual foraminifera to assess the relative magnitude of hydrographic change at discrete periods in Earth’s past (Thirumalai et al., 2013). Owing to the approximately four-week life span of an average foraminifer, the geochemical signature of a single fossil foraminiferal test represents a monthly “snapshot” of the ambient environmental conditions in which the organism precipitated its shell (Spero, 1998). Therefore, intraspecific variations in the trace element composition of foraminiferal populations represent a composite sample of hydrographic variability at the timescale represented by a single stratigraphic interval (Billups and Spero, 1996; Thirumalai et al., 2013). In regions of the global ocean where hydrographic variability is dominated by a particular climate oscillation (e.g. ENSO), IFA-based techniques can be used to resolve differences in the strength of that oscillation through time.

Although the IFA technique has been applied to sediment cores from ENSO-sensitive regions in the past, inconsistencies surrounding patterns of ENSO behavior persist (Koutavas et al., 2006; Leduc et al., 2009b; Koutavas and Joanides, 2012; Ford et al., 2015; White et al., 2017). The discrepancy among these IFA reconstructions could stem from the inherent complexity of the coupled ocean-atmosphere system of the tropical Pacific, a notably dynamic region of the global ocean (Fiedler and Talley, 2006). More likely, however, is that the ambiguous history offered on paleo-ENSO is a byproduct of differences in each study's respective methodology. Efforts to successfully deconvolve the ENSO-related signal from the "noise" of the ambient background climate are highly sensitive to methodological parameters such as foraminiferal species (surface- vs. subsurface-dwelling foraminifera), geochemical proxy (Mg/Ca paleothermometry, $\delta^{18}O$, etc.), and statistical treatment (parametric vs. non-parametric measures of scale). For example, IFA-based reconstructions on surface-dwelling foraminifera could lead to erroneous conclusions of paleo-ENSO by virtue of the fact that the variability in the surface ocean is governed, to first order, by the annual cycle (Thirumalai et al., 2013). Furthermore, proxies such as $\delta^{18}O$, which incorporate a mixed signal of temperature, salinity, and continental ice volume, could introduce additional variability into IFA populations that mask the ENSO-related signal. The use of proxies with more direct proxy-parameter relationships (e.g.

foraminiferal Mg/Ca) could circumvent this issue. Finally, the detection of changes in paleo-ENSO using IFA depends upon resolving minute differences among reconstructed paleotemperature distributions, requiring the use of more robust and resistant statistical methods over more traditional, parametric alternatives (e.g. standard deviation and variance) (Khider et al., 2011; Ford et al., 2015). Altogether, careful methodological and statistical considerations are necessary to ensure that the reconstructed signals (and their attendant differences) can appropriately be attributed to paleo-ENSO variation.

In this study, I present new Mg/Ca-based records of long-term subsurface temperature change (via conventional multi-shell analyses) and subsurface temperature variability (via IFA) using subsurface-dwelling foraminifera *Neogloboquadrina dutertrei* from a high-sedimentation rate piston core (MV1014-02-17JC; 00° 10.83'S, 85° 52.00'W; 2867 m depth) and its corresponding multi-core (MV1014-02-09MC; 00° 41.63'S, 85° 20.00'W; 2452 m depth). Both cores were recovered from the cold tongue of the eastern equatorial Pacific (EEP), a region which experiences significant hydrographic variability associated with the ENSO. The IFA record of subsurface temperature variability, interpreted as a record of ENSO variability, was generated for seven targeted time slices spanning the Holocene, LGM, and the millennial-scale oscillations of the last deglaciation. I also developed a bootstrap Monte Carlo algorithm which, by manipulating modern observations to simulate hypothetical scenarios of ENSO change, tested the efficacy and sensitivity of two statistical methods previously applied to IFA reconstructions: biweight estimation and quantile-quantile analysis. Taken together, the data presented here offer a detailed account of paleo-ENSO evolution over the last 25 kyrs. My new record fills critical data gaps in our knowledge of ENSO history, particularly over the last deglaciation, and brings together records of tropical Pacific climatology to better understand the predominant forces and feedbacks that governed ENSO behavior across the last 25 kyrs.

2. Regional Setting

2.1 Oceanography of the Eastern Equatorial Pacific

Piston core MV1014-02-17JC and multi-core MV1014-02-09MC (hereafter 17JC and 09MC, respectively) were recovered from the Carnegie Ridge east of the Galápagos archipelago during research cruise MV1014 on the R/V *Melville* in 2010 (Figure 1). Both cores were collected from the heart of the equatorial cold tongue, a prominent hydrographic feature of the tropical Pacific established by trade wind-induced upwelling of cold, nutrient-rich waters along the coast of South and Central America and extending westward along the equator to ~120°W (Fiedler and Talley, 2006). As a result of this upwelling, the EEP is characterized by a shallow mixed layer ~15 m in depth (Locarnini et al., 2013) and a prominent thermocline (Fiedler and Talley, 2006; Figure 1). Annual fluctuations in upwelling strength are governed by the latitudinal migration of the Intertropical Convergence Zone (ITCZ). The ITCZ tracks the displacement of the thermal equator to the north during boreal summer, strengthening the southeasterly trade winds at the study site and enhancing Eckman-induced divergence along the equator (Schneider et al., 2014). During boreal winter, the ITCZ migrates south, reducing the cross-equatorial flow of the southeast trades and weakening overall upwelling intensity (Schneider et al., 2014; Waliser and Gautier, 1993). Consequently, SSTs at the study site range annually from 23.0°C to 26.1°C, with an average of 24.1°C (Locarnini et al., 2013).

At depth, the EEP subsurface is bathed in waters delivered to the region by the strong, semi-permanent Equatorial Undercurrent (EUC; Figure 1). The EUC flows eastward at the base of the equatorial thermocline, gradually shoaling on approach to the EEP (Nie et al., 2019;

Johnson et al., 2002; Kessler, 2006). EUC waters are sourced from the western Pacific margin north of New Guinea Island, where intermediate water masses originating from the Southern Ocean converge with waters from the North Pacific (Tsuchiya et al., 1989). However, along its path to the EEP, the EUC is increasingly diluted from its original composition by meridional circulation cells delivering warm, saline subtropical surface waters to the equatorial subsurface (Nie et al., 2019; Fielder and Talley, 2006; Johnson and McPhaden, 1999). At its eastern terminus, the EUC is effectively obstructed from the Central American coast by the Galápagos (Lukas, 1986; Karnauskas et al., 2010); however, observations east of 95°W suggests that at least portions of the EUC circumvent the islands and occupy subsurface waters above the Carnegie Ridge (Lukas, 1986; Tsuchiya and Talley, 1998). Upon collision with the Galápagos, the EUC bifurcates: one branch flows south to join the Peru-Chile Undercurrent and another branch surpasses the islands to the north and continues east towards the coast (Lukas, 1986; Tsuchiya and Talley, 1998; Kessler, 2006; Karnauskas et al., 2006). Some of the waters from the northern branch are brought to the surface as part of the EEP upwelling regime before they are recirculated north into the equatorial surface current system (Lukas, 1986; Kessler, 2006).

On a basin-wide scale, the expression of cold SSTs in the east is contrasted by the displacement of warm surface waters to the west, which amass east of the Indonesian archipelago and form a warm pool encompassing roughly 18% of the total surface area of the Pacific Ocean (De Deckker, 2016). The substantial contrast in surface hydrography between the warm pool and the cold tongue generates one of the strongest equatorial SST gradients in the world (Jin, 1996) and imparts a significant influence on tropical atmospheric circulation (Bjerknes, 1969). In the west, the warm pool serves as a large, monolithic source of heat and water vapor to the overlying atmosphere, forming the foundation of a large atmospheric convection cell that drives the zonal Walker circulation (Bjerknes, 1969). The strength of the Walker circulation governs the strength of the trade winds, which in turn sustains the zonal asymmetry in tropical Pacific SSTs by maintaining upwelling intensity in the equatorial cold tongue (Bjerknes, 1966; Jin, 1996). This positive feedback loop, known as the Bjerknes feedback, is perturbed on interannual timescales by quasi-periodic fluctuations in sea level pressure in the western and central Pacific. The oscillation of high- and low-pressure systems over the west-central Pacific lead to a westerly trade wind anomaly that destabilizes the equilibrium state of the coupled ocean-atmosphere system, giving rise to the natural instability which constitutes the ENSO system (Bjerknes, 1966; Jin, 1996; Liu and Huang, 1997). During a warm ENSO phase (El Niño), the weakening of the easterly trades relaxes the zonal SST gradient by allowing warm waters in the west to propagate eastward, deepening the thermocline in the EEP (Wang and Fielder, 2006). The opposite occurs during an ENSO cold phase (La Niña), where an intensification of the trade winds strengthens the zonal SST gradient, enhances upwelling in the cold tongue, and shoals the EEP thermocline near the surface.

As a consequence of the large-scale changes that occur in the EEP during the alternate phases of ENSO, regional seawater temperature patterns exhibit a strong interannual character that, particularly within the shallow subsurface, dominate over other first-order climate signals such as seasonality (Wang and Fiedler, 2006; Fiedler and Talley, 2006). 26 years of modern hydrographic data collected by a nearby National Oceanic and Atmospheric Administration (NOAA) Tropical Atmosphere Ocean (TAO) Array buoy (0°N 95°W; yellow hexagon in Figure 1) illustrate this point clearly (Figure 2a). EEP SST variability closely adheres to the annual cycle and is relatively poorly correlated to both atmospheric (Southern Oscillation Index; SOI) and oceanic indices of ENSO (Niño 3.4 SST Anomaly). Occasional warm anomalies associated with El Niño events do punctuate the sea surface monthly time series (Figures 2a), but the influence of the seasonal cycle on overall EEP SST variability exceeds the influence of interannual cycles like ENSO by nearly 2:1 (Wang and Fiedler, 2006). Critically, the influence of seasonality on regional ocean temperatures attenuates with depth, yielding to stronger interannual influences such as ENSO (Figure 2a). EEP subsurface waters experience large warming anomalies associated with the vertical migration of the regional thermocline at the onset of El Niño events. During exceptionally strong events, such as the 1997/98 El Niño, the thermocline can deepen by as much as 70 m (Jacox et al., 2016), producing a subsurface warming anomaly of nearly 10°C as deep as 120 m below the surface (Figure 2a). At ~40 – 80 m depth, correlations between the TAO observations and both indices of ENSO are at their greatest (Figure 2a) and interannual temperature excursions exceed seasonal anomalies by a factor of six (Figures 2b and 2c). In light of this strong link between the EEP subsurface and ENSO, it follows that geochemical and paleoceanographic techniques employed to reconstruct subsurface temperature variability can be used to assess relative changes in the amplitude of ENSO through time.

2.2. *Neogloboquadrina dutertrei* as a Recorder of Subsurface Temperature Variability

N. dutertrei is a non-spinose, symbiont-bearing planktic foraminifera that dominates living foraminiferal assemblages in the modern-day EEP (Fairbanks et al., 1982). *N. dutertrei* can tolerate a broad spectrum of temperatures and salinities (between 13 – 33°C and 25 – 46 psu, respectively) which allows it to thrive in exceptionally dynamic regions of the global ocean such as the EEP (Schiebel and Hemleben, 2017). A combination of plankton tow (Fairbanks et al., 1982) and sediment trap studies (Curry et al., 1983; Thunell and Reynolds, 1984; Faul et al., 2000) from the tropical Pacific ascribe a wide range of calcification depths to the thermocline-dwelling species, spanning ~25 – 160 m water depth. Peak abundances, however, tend to cluster at depths corresponding to the subsurface chlorophyll maximum layer (Fairbanks et al., 1982). Core-top material from sample sites along the Carnegie Ridge further refine estimates of *N. dutertrei* depth habitat to ~40 – 75 m near the core site (Loubere, 2001), placing its depth habitat squarely within the zone of maximum temperature anomalies associated with ENSO (scale bar in Figures 2b and 2c).

Nevertheless, some concern has been expressed as to the viability of *N. dutertrei* to faithfully record ENSO variability in the EEP (Zhu et al., 2017; Ford et al., 2018). This criticism draws upon previous ecological work in the region suggesting that *N. dutertrei* shifts its mean depth habitat in response to changes in thermocline depth on seasonal and longer timescales (Sautter and Thunell, 1991). A shifting mean depth habitat in response to a temporally-varying thermocline could, in effect, "smooth" the variability recorded by individual foraminiferal populations preserved in marine sediments. In other words, temperature anomalies observed about a time-variant mean thermocline depth (i.e. a Lagrangian perspective) would be less variable than temperature anomalies observed from a fixed depth in the water column (i.e. a Eulerian perspective) (Zhu et al., 2017).

However, data from core-top populations of *N. dutertrei* throughout the Pacific basin suggest that this is not an issue on sub-millennial timescales. Mg/Ca-derived subsurface temperature distributions from sediment core-tops (which integrate fossil foraminifera spanning centuries of time) are consistent with subsurface temperature variability in both modern observations and climate reanalysis datasets (Rongstad et al., 2018; White et al., 2017). On glacial-interglacial timescales, however, the effect of a vertically migrating thermocline on the shape of paleotemperature distributions is less clear. If thermocline variability on sub-millennial timescales does not significantly affect the spread of paleotemperature distributions, the only types of variability that remain are millennial-scale adjustments in thermocline depth in response to abrupt climate events (such as the those which characterize the last deglaciation) and the long-term secular trend associated with glacial-interglacial climate change (Ford et al., 2018). I argue that any migration of *N. dutertrei* in response to these trends in thermocline depth would likely have little influence over the shape of paleotemperature distributions recovered from sediment cores with a sufficiently high sedimentation rate (i.e. high time resolution) such as core 17JC. Provided that a single stratigraphic interval from 17JC represents ~80 yrs of integrated hydrographic variability (see section 3.1.1), both glacial-interglacial and millennial-scale trends in thermocline depth are likely contributing very little to the variability recorded by IFA populations within that window of time. I therefore argue that population-wide migrations in habitat depth related to shifts in thermocline depth do not pose an issue for my reconstructions of subsurface temperature variability.

3. Materials and Methods

3.1 Analytical Techniques

3.1.1 Age Model Development

The age model for 17JC for the time period under investigation (0 – 25 kyrs) is constrained by six radiocarbon dates and one $\delta^{18}O$ tie point to NGRIP at the MIS 1 – 2 transition (Figure 3). I assume the core-top of 17JC is similar in age to the core-top of nearby multi-core 09MC, dated at 2.20 ± 0.12 kyrs. The average sedimentation rate for the upper 333 cm of 17JC is ~12 cm kyr^{-1} based on linear interpolation between radiocarbon dates and oxygen isotope tie points, equating to an average age resolution of ~80 yrs cm^{-1}. Radiocarbon analyses were performed at the National Ocean Sciences Accelerator Mass Spectrometry facility (NOSAMS) at

Woods Hole Oceanographic Institution, and ages were subsequently converted to calendar ages using the CALIB 7.1 software (Stuiver et al., 2018) and the Marine13 calibration dataset (Reimer et al., 2013) with a standard marine reservoir correction of 400 years (Loveley et al., 2017).

3.1.2 Multi-shell Minor and Trace Element Analyses

I estimate long-term changes in tropical Pacific subsurface hydrography by generating a down-core temperature record using conventional multi-shell Mg/Ca analyses on *N. dutertrei*. Freeze-dried sediment from 17JC was disaggregated in ultra-pure water, wet-sieved through a 63 µm mesh to eliminate fine clays, and oven dried at 50°C. Enough shell material for duplicate analyses (~600 µg or 10–14 shells) was picked at 4 cm intervals spanning 0 – 333 cm, corresponding to a sampling resolution of ~300 yrs. All core intervals were duplicated at least once, with 12% of intervals run in triplicate or quadruplicate. To avoid intraspecific variation in Mg/Ca ratios, *N. dutertrei* were only selected from the 400 – 450 µm size fraction. *N. dutertrei* sink to deeper depths and add a crust of gametogenic calcite towards the end of their life cycle that can bias shell chemistry to colder temperatures (Hemleben et al., 1977; Sautter, 1998; Spero et al., 2003), so specimens with observable calcite crusts were not selected for geochemical analysis. Picked foraminifera were gently crushed between two glass plates, homogenized, split into two equal aliquots, and cleaned for trace metal analyses following a protocol described by Schmidt et al. (2012a). In brief, samples are (1) sonicated for 15 – 20 seconds in ultra-pure water (5x) and methanol (2x) to remove clays; (2) exposed to treatments of hot reducing and oxidizing solutions to eliminate diagenetic coatings and organic matter, respectively; (3) transferred into new acid-leached micro-centrifuge vials; and (4) leached with a weak, ultra-pure 0.001N HNO_3 solution. All clean work was conducted in laminar flow benches under trace metal clean conditions.

Cleaned samples were dissolved in 2% HNO_3 and analyzed via isotope dilution on a Thermo Scientific Element XR High Resolution Inductively Coupled Plasma Mass Spectrometer (HR-ICP-MS) at Old Dominion University's College of Sciences Major Instrumentation Cluster (COSMIC). A suite of trace and minor elements were analyzed and normalized to Ca, including Mg, Sr, Na, Ba, Al, Mn, and Fe. Analyses that returned low percent recovery (<15%) or high Al/Ca, Fe/Ca, or Mn/Ca ratios (>150 µmol/mol) were rejected. Al/Ca, Fe/Ca, and Mn/Ca ratios are used to monitor cleaning efficiency: elevated Al/Ca ratios indicate the presence of detrital clays not removed during the cleaning process, and high levels of Fe/Ca and Mn/Ca indicate the presence of remnant authigenic coatings. Poor coefficients of determination (r^2) suggested that neither the cleaning indicators nor the average shell weight estimates sufficiently explained the variability observed in the multi-shell Mg/Ca record (Figure 4a – d). Based on repeated measurement of a synthetic matrix-matched standard, the long-term analytical precision of Mg/Ca ratios across all runs was ±1.60% or ±0.055 mmol/mol (n = 42).

3.1.3 Individual Foraminiferal Analysis

I investigate changes in paleo-ENSO variability by performing Mg/Ca analyses on single specimens of *N. dutertrei* (n = 517) within specifically targeted stratigraphic intervals from both 17JC and 09MC. Down-core time slices sampled from 17JC span six discrete time horizons: the Mid-Holocene (MH), the Early Holocene (EH), the Younger Dryas (YD), the Bølling-Allerød (BA), Heinrich Stadial 1 (HS1), and the LGM (see Table 1). The core-top of 09MC was selected to represent a composite sample of hydrographic variability covering both the modern era and Late Holocene (Modern/LH). The extent to which the Modern/LH time slice represents modern hydrographic variability is explored in Section 4.4. For each time slice, I picked and processed approximately 74 (± 5) individual *N. dutertrei* shells, a sample size which is demonstrated in a prior sensitivity study to adequately approximate true hydrographic variability (Thirumalai et al., 2013). All individuals were selected from the 450 – 500 μm size fraction. The slightly larger size fraction of the IFA samples compared with the multi-shell analyses (400 – 450 μm) was chosen to ensure enough sample material was available for each analysis.

In preparation for cleaning, individual *N. dutertrei* shells were loaded into micro-centrifuge vials whole, immersed in ultra-pure water, and gently crushed with a fine plastic rod to open the chambers. The cleaning procedure for individual foraminifera is similar to the method described above for multi-shell samples with some notable modifications: (1) I centrifuged samples at 7000 rpm for 60 seconds to concentrate calcite fragments at the bottom of the vials before transferring to acid-cleaned vials; and (2) I eliminated the reductive step and the final weak acid leach to minimize sample loss that typically results from interaction with corrosive chemical agents (Barker et al., 2003). As a consequence of the latter alteration, I can expect the multi-shell Mg/Ca ratios to be approximately 10 – 15% lower than the mean of the IFA Mg/Ca ratios owing to the preferential dissolution of Mg-rich calcite during the reductive and acid leach steps (Barker et al., 2003). I do not, however, expect the alterations in the cleaning procedure to affect the overall spread of the IFA data under the assumption that post-depositional processes that modify Mg/Ca (dissolution, precipitation of ferromanganese coatings, etc.) act uniformly and consistently across the cross-sectional area of the core. A study from the Ontong Java Plateau reinforces this assumption with regards to dissolution (Rongstad et al., 2017), demonstrating that the distributional shape of paleotemperatures derived from individual foraminifera is preserved even in partially dissolved sediments.

I employed a standard external calibration method detailed by Marchitto et al. (2006) for my individual Mg/Ca analyses. Cleaned foraminiferal samples were dissolved in 500 μL of 2%

HNO_3 before each sample run. Three mother standards (S1 – S3) were prepared gravimetrically at 120 ppm Ca in a 2% HNO_3 matrix with added concentrations of Al, Mn, and Fe that mimic the range and proportions found in a typical foraminifer. For each sample run, standards were diluted 10x to a concentration of 12 ppm Ca, roughly equivalent to the weight of one post-cleaning *N. dutertrei* (15 µg $CaCO_3$). The three calibration standards and two blanks consisting of the same 2% HNO_3 used to dilute standards and samples were spaced every six samples in the run sequence. All raw metal intensities were blank- and drift-corrected and normalized to Ca. Standard calibration curves were generated by linear regression between the ratio of observed count intensities and the known Metal/Ca ratios for each standard. Out of 157 total Mg/Ca calibration curves, almost all (94%) generated r^2 values over 0.999 (17% $\geq$ 0.9999) and were never lower than 0.99. Long-term analytical precision (1σ) across all runs spanning several months was 2.61%, 1.28%, and 0.88% for three gravimetrically-prepared consistency standards (C1 – C3) with known Mg/Ca ratios of 0.803, 1.419, and 2.034 mmol/mol, respectively (n = 18). The majority of Mg/Ca ratios measured from individual foraminifera (65%) fall within the range of C1 and C2, and 31% fall below the ratio of C1. As with the multi-shell record, I monitored Al/Ca, Fe/Ca, and Mn/Ca ratios as cleaning indicators. I also monitored ^{43}Ca intensities as an indicator of sample size. Neither the cleaning indicators nor estimated sample size sufficiently explained the variability observed in the IFA Mg/Ca dataset (Figure 4e – h).

3.1.4 Calculating Subsurface Temperatures

Culturing experiments (Nürnberg et al., 1996; Lea et al., 1999; Russell et al., 2004; Hönisch et al. 2013; Allen et al., 2016), core-top calibrations (Rosenthal et al., 1997; Elderfield and Ganssen, 2000; Dekens et al., 2002; Regenberg et al., 2009), and sediment trap studies (Anand et al., 2003; McConnell and Thunell, 2005) have demonstrated that temperature exerts a first-order control on the Mg/Ca ratio of foraminiferal calcite, with minor contributions from salinity (Hönisch et al. 2013; Hertzberg and Schmidt, 2013) and pH (Lea et al., 1999; Allen et al., 2016). I compute subsurface temperatures at the core site for both the conventional down-core Mg/Ca record and the IFA populations using a regional, species-specific calibration developed from Pacific core-top samples by Dekens et al. (2002):

$$\text{Mg/Ca} = 0.60 \exp 0.08(T - 2.8(\text{core depth in km}) - 5.4°\text{C}) \tag{1}$$

Some minor signs of partial dissolution (soft foraminiferal tests) justified the inclusion of a dissolution correction term, appended to the exponential constant in equation (1) as a function of core depth (Dekens et al., 2002). Inclusion of the correction term yields a subsurface temperature value from 09MC core-top material (averaged from the Modern/LH IFA population) that is identical to average modern EEP temperatures at 40 m depth (19.5°C). Likewise, application of equation (1) to core-top material from 17JC generates a subsurface temperature value (20.4°C) that is consistent, within error, with modern observations. The 1σ error accompanying the calibration above equates to ±1.6°C (Dekens et al., 2002). Taken together with analytical uncertainty, the compounded error for each calculated subsurface temperature value is ±2.4°C.

3.1.5 Stable Isotope Analysis and Calculating Ice Volume Free-$\delta^{18}O_{SW}$

The stable isotope data from 17JC presented in this thesis were originally published in Loveley et al. (2017). In preparation for analysis, *N. dutertrei* from the >250 μm size fraction were picked at 2 cm intervals and briefly sonicated in methanol. Analyses were performed on a Thermo Scientific MAT 253 dual-inlet stable isotope ratio mass spectrometer (IR-MS) coupled to a Thermo Scientific Kiel IV automated carbonate device at the Stable Isotope Geosciences Facility at Texas A&M University. Calculated oxygen and carbon isotope values are reported in delta notation relative to the Vienna Pee Dee Belemnite (VPDB) standard. Long-term analytical precision, based on the measurement of the NBS19 analytical standard within each run, is ±0.06‰.

The $\delta^{18}O$ signature of fossil foraminiferal calcite ($\delta^{18}O_C$) is influenced by the temperature and $\delta^{18}O$ composition of the ambient seawater ($\delta^{18}O_{SW}$) in which the shell is precipitated, the latter being a function of changes in regional salinity and, on glacial-interglacial timescales, changes in continental ice volume (Shackleton, 1987; Schmidt et al., 2004). I utilize independent estimates of temperature and ice volume change to parse the salinity component from the 17JC $\delta^{18}O_C$ signal and establish a proxy record of relative salinity change in the EEP subsurface through time. First, I account for the temperature component by removing the Mg/Ca-derived subsurface temperatures from the $\delta^{18}O_C$ record. Because the original stable isotope record by Loveley et al. (2017) was sampled at a higher resolution and at different time steps than the multi-shell Mg/Ca record, I linearly interpolate the original $\delta^{18}O_C$ record and index the values from depths which correspond to the Mg/Ca-derived temperature data. I then use the $\delta^{18}O_C$ – Mg/Ca paleotemperature pairs to solve for $\delta^{18}O_{SW}$ using the following equation (Bemis et al., 1998):

$$T\,(^\circ C) = 16.5 - 4.80\,(\delta^{18}O_C - (\delta^{18}O_{SW} - 0.27‰)\,) \tag{2}$$

Next, I corrected for variations in continental ice volume with reference to a high-resolution record of eustatic sea level over the last glacial termination (Lambeck et al., 2014) assuming the ~120 m difference in glacial-interglacial sea levels corresponds to a 1.05‰ change in global $\delta^{18}O_{SW}$ (Schrag et al., 2002). The remaining ice volume free $\delta^{18}O_{SW}$ signal (IVF-$\delta^{18}O_{SW}$) primarily reflects relative changes in regional salinity. The error surrounding the calculated IVF-$\delta^{18}O_{SW}$ record was estimated using the Paleo-Seawater Uncertainty Solver (PSU Solver; Thirumalai et al., 2016). The program propagates the 1σ analytical uncertainty from the $\delta^{18}O_C$

and Mg/Ca measurements, the calibration error on equations (1) and (2), and the uncertainty in the sea level reconstruction (Lambeck et al., 2014) to generate a total error of approximately ±0.23‰.

3.2 Statistical Approach

In previous IFA-based studies (Koutavas et al., 2006; Koutavas and Joanides, 2012; Leduc et al., 2009; Sadekov et al., 2013), relative differences in past upper ocean hydrographic variability were inferred through direct comparisons of conventional scale estimators such as standard deviation and variance. The problem with this approach, however, is that it relies on *a priori* assumptions regarding the normality of the underlying climate signal (Lanzante, 1996; Khider et al., 2011). Given the differences in amplitude between El Niño and La Niña events (An et al., 2004; Choi et al., 2011) and the subsequent asymmetry in the EEP subsurface temperature response (Figures 2a and 2c), both modern and IFA-derived temperature distributions are likely to be non-gaussian in nature. Furthermore, the presence of outlying values in an IFA dataset could significantly distort parametric measures of scale and compromise the ability to draw accurate inferences regarding paleo-ENSO strength (Lanzante, 1996; Khider et al., 2011). In light of these facts, I feel that the use of parametric scale estimators is inappropriate in the present case. Instead, I use a combination of robust biweight estimates of spread, specifically the biweight standard deviation (BSD), and quantile-quantile (Q-Q) analysis to investigate relative differences between the paleotemperature distributions of my sampled time slices.

The benefit of using BSD over other parametric alternatives lay in its inherent resistance to the presence of outliers (Lanzante, 1996). Khider et al. (2011) were the first to recognize the utility of BSDs in evaluating paleo-ENSO intensity and applied the technique to their IFA dataset from the Sulawesi Sea. First, calculating BSD involves determining the median and median absolute deviation for each IFA population. These estimators are then used to build an internal weighting function that modifies the "influence" of each paleotemperature value as a function of proximity to the median (Hoaglin et al., 1983; Lanzante, 1996; Khider et al., 2011; Rongstad et al., 2017). In effect, the weighting function places more emphasis on values close to the center of a distribution, decreasing outwards until, at some distance prescribed by a censor value (c), the weighting function goes to zero. For the purposes of my analysis, I define c to be 7.5 (a conventional value), placing this threshold at 5σ (Lanzante et al., 1996). I test for significant differences between my time slices using the two-sample Kolmogorov-Smirnov Goodness-of-fit Test (Massey, 1951) and the Brown-Forsythe Test for Homogeneity of Variance (Brown and Forsythe, 1974). The two-sample Kolmogorov-Smirnov test assesses the null hypothesis that two sample distributions come from the same general population distribution (sensitive to both location and scale). The Brown-Forsythe test is a non-parametric equivalent to the Bartlett Test and tests the null hypothesis that two randomly-sampled time slices come from homoscedastic population distributions (equal in spread) (Brown and Forsythe, 1974).

However, in some cases it is possible that the outliers being muted in the BSD computation are not necessarily atypical and constitute a part of the natural climate signal. For instance, El Niño-forced warming anomalies at the core location can reach temperatures ≥26°C, far exceeding the average subsurface temperature of 19.5°C. A random sampling of individual foraminifera would invariably produce at least one individual that lived during these events and would appear in the paleotemperature distributions as an "outlier" despite faithfully representing oceanographic conditions at the time. Hence, BSD may not be an ideal tool for extracting insights regarding the ENSO system, at least at the present study location. Therefore, I complement the BSD calculations with Q-Q analyses of each down-core IFA population. Q-Q plots are a powerful data visualization tool that allows for the direct comparison of quantiles from one distribution against the equivalent quantiles of another (Ford et al., 2015; White et al., 2017). First, empirical cumulative distribution functions (ECDFs) were constructed for each IFA population and interpolated at 2% intervals to generate 50 equally spaced quantiles. Subsequent Q-Q comparisons were done graphically. If two distributions are identical in both location and scale, the quantiles plot along a 1:1 line. Distributions that differ in the mean but maintain a similar spread plot along a parallel 1:1 line offset by the difference between the two means. Relative differences in the spread, kurtosis, and skewness of the underlying distributions draw the quantiles away from these reference lines and change the overall slope of the plotted quantiles.

To make these qualitative comparisons more statistically robust, I adopted a strategy pioneered by Ford et al. (2015) and utilized a bootstrapping technique to simulate the uncertainty in Q-Q analysis related to sampling of the population distribution (see also White et al., 2017). ECDFs were generated for each of the populations plotted along the y-axis and, assuming the ECDF to be a continuous function, a Monte Carlo resampling scheme created 10,000 new subsamplings made up of 70 randomly-selected points along the ECDF. Quantiles were computed for each Monte Carlo dataset and sorted such that all 10,000 values for each quantile were arranged from coldest to warmest. Finally, I eliminated the 500 coldest and warmest values (top and bottom 5%) to create a final set of 9000 values for each quantile that collectively represent 90% confidence bounds (in the y-direction). Thus, if a quantile diverged from the 1:1 line beyond its confidence bounds, it is considered significantly different at the 90% confidence level. All data manipulation and statistical analyses were conducted using MATLAB v.9.5 R2018b.

3.3 Bootstrap Sensitivity Analysis

A case can be made that some of the disparity between the narratives offered on paleo-ENSO by previous IFA-based studies can be attributed to differences in statistical treatment (see, e.g., Rustic et al., 2015 vs. Khider et al., 2011 for the last millennium, or Koutavas and Joanides, 2012 vs. Ford et al., 2015 for the LGM). Therefore, an important aspect of this study is to simultaneously constrain the uncertainties related to IFA sampling for each of my chosen statistical tools (BSD and Q-Q analysis) and assess their respective sensitivity to prescribed changes in ENSO amplitude. To that end, I develop a bootstrap sensitivity algorithm that seeks to establish a minimum threshold at which a certain degree of ENSO change begins to register in IFA-derived statistics as a significant result (i.e. to what degree does the ENSO have to change in order for me to "see" it in my statistical analysis). The algorithm is largely inspired by the Individual Foraminiferal Approach Uncertainty Analysis (INFAUNAL) model developed by Thirumalai et al. (2013) and previous IFA sensitivity analyses performed by Ford et al. (2015) and White et al. (2017). First, the algorithm is fed an environmental time series, in this case the TAO temperature time series at 40 m (red box in Figure 2a), and uses a continuous wavelet transform function to build a 2 – 7 year band-pass filter and extract the ENSO-related signal from the input data series (Torrence and Compo, 1998; function by J. Emile-Geay, accessed at https://github.com/CommonClimate/common-climate/blob/master/wavelet_filter.m). I select the TAO data from 40 m as the input given the strong correlation to both the SOI and Niño 3.4 SST Anomaly (Figure 2a), as well as its location within the upper portion of the *N. dutertrei* depth habitat. The amplitude of the newly-extracted ENSO frequency is then manipulated to varying degrees and added back into the residual time series data to create 20 new synthetic time series: 10 scenarios in which the ENSO is dampened and 10 scenarios in which it is amplified. Each scenario represents a 10% incremental change in the amplitude of ENSO, ranging from 100% dampened (or no ENSO) to 100% amplified (or 2x ENSO). These new time series are combined with the original TAO time series (hereafter the “non-adjusted” scenario) for a total of 21 modeled ENSO scenarios.

Built within the sensitivity model is a Monte Carlo resampling scheme that simulates the random sampling of individual foraminifera. Each of the 21 time series represent an idealized virtual sediment sample (i.e. a perfectly preserved signal entrained within a single stratigraphic interval) and the monthly mean temperature data which constitute the time series are representative of “foraminifera” that lived during that time. The resampling scheme generates 10,000 pseudo-IFA populations by selecting (with replacement) 70 individual temperature values along the time series. The algorithm then computes the BSD for each of the 10,000 pseudo-IFA populations and generates histograms with 95% confidence bounds for each scenario to illustrate the uncertainty inherent to random IFA sampling. Each pseudo-IFA population is also subjected to Q-Q analysis and compared against a reference population randomly generated from the non-adjusted ENSO scenario at the beginning of the model run. The algorithm searches the quantiles for any significant deviation from the mean-adjusted 1:1 line and assigns a simple logical value to each: +1 if the quantile is significantly above the reference line, -1 if the quantile is significantly below the reference line, and 0 if the reference line is within the 90% confidence bounds. The model then calculates what proportion of the 10,000 subsamplings produced a +1 and a -1 for each quantile. The process above is executed for each scenario, beginning with the 100% dampened ENSO scenario and moving systematically along the spectrum of scenarios before concluding with the 100% amplified ENSO scenario. In the end, the algorithm outputs 10,000 BSD values and 100 Q-Q probabilities for each of the 21 scenarios.

4. Results

4.1 Subsurface Temperature and Salinity Records

The down-core 17JC Mg/Ca-derived subsurface temperature record calculated from equation (1) and the IVF-$\delta^{18}O_{SW}$ record computed from equation (2) are both presented in Figure 5. Bulk Mg/Ca values range from 0.66 to 1.18 mmol/mol, corresponding to a range of calcification temperatures between 14.4 and 21.7°C, and IVF-$\delta^{18}O_{SW}$ values from 0.38 to 1.57‰. The patterns exhibited by the down-core records illustrate prominent glacial-interglacial differences in EEP subsurface conditions with some notable changes in response to millennial-scale climate events. Between 19.2 and 18.5 kyrs, the 17JC subsurface temperature record indicates an abrupt, stepwise transition from an average glacial temperature of 15.8°C (±1.1°C) to an average of 19.0°C (±1.1°C) across the Holocene and deglaciation (Figure 5a). The magnitude of this warming (3.2°C) is robust, exceeding the compounded error on the subsurface temperature calculations. The rise in subsurface temperature is also associated with a coincident increase in IVF-$\delta^{18}O_{SW}$ of 0.95‰ (Figure 5b), marking the transition from a cooler, fresher EEP subsurface during the LGM to a warmer and saltier subsurface during the deglacial period. This abrupt transition at ~19 kyrs marks the beginning of a positive temperature/salinity excursion associated with HS1. Subsurface temperatures and IVF-$\delta^{18}O_{SW}$ maintain an average of 19.2°C (±0.7°C) and 1.35‰ (±0.2‰) across HS1, respectively, before abruptly decreasing at the termination of HS1. Between 14.6 to 14.4 kyrs, subsurface temperatures cool 2.1°C and salinity decreases as northern hemisphere climate transitions from HS1 to the BA. EEP subsurface conditions remain relatively cool/less saline for ~0.5 kyrs before beginning a gradual transition at ~14 kyrs into the YD. Here, the covariance between subsurface temperature and salinity decouples. The end of the YD is marked by an abrupt temperature decrease that is not associated with an accompanying salinity change. This remains true for the Holocene portion of the record. Subsurface temperature variability in the early and late Holocene is equal in magnitude to the changes that occur across the deglaciation, while conditions during the mid-Holocene (6.9 to 4.3 kyrs) are more stable. In the IVF-$\delta^{18}O_{SW}$ record, the Holocene is characterized by a gradual decrease in salinity across the early and mid-Holocene (from 10.8 to 3.3 kyrs) before increasing slightly in the youngest part of the record.

4.2 Sensitivity Model Results

Before applying the chosen statistical tools (BSD and Q-Q analysis) to the IFA dataset from the EEP, I first examined the relative sensitivity of each method by scrutinizing the output of the bootstrap sensitivity algorithm. The mean BSD for each ENSO scenario, calculated by averaging the 10,000 estimated BSDs from the pseudo-IFA populations, range from 1.96 (100% dampened ENSO) to 3.84°C (100% amplified ENSO). Mean BSDs consistently estimate the "true" environmental variability (i.e. the calculated BSD on the full synthetic time series of that scenario) with a precision of ≤1% (Table 2). Despite this close agreement, the total range of BSDs within a given scenario, and by extension the derived 95% confidence limits, were very broad and increased as the variability of the synthetic temperature time series increased. Put simply, estimates of sampling uncertainty scale as a function of ENSO amplitude. 95% confidence limits were most reduced for the 100% dampened ENSO scenario (±0.15°C or ±7.6%) and were greatest for the 100% amplified ENSO scenario (±0.43°C or ±11.2%). In comparison, the uncertainty in BSD estimates for the non-adjusted ENSO scenario (i.e. the unaltered TAO temperature time series at 40 m) was ±0.25°C (±9.2%). Given these broad uncertainties related to IFA sampling, moderately prescribed changes in ENSO amplitude (10 – 50%) are not easily distinguishable using the BSD method. The minimum threshold at which

BSD estimates could successfully detect an increase (decrease) in ENSO intensity with 95% confidence was a 60% amplification (50% reduction) in ENSO amplitude relative to the non-adjusted scenario (Figure 6).

Q-Q analyses of the pseudo-IFA populations revealed that the impact of varying ENSO amplitude was primarily localized in the tails of the simulated temperature distributions. As such, changes in ENSO amplitude registered in Q-Q plots as changes in the slope of the warmest and coldest quantiles. However, in assessing the sensitivity of the Q-Q method to prescribed changes in ENSO, I limited my analysis of the model output to the three warmest quantiles (48th – 50th quantiles; Figure 7) for two reasons. First, quantiles computed from the TAO observations at 40 m indicated that the 49th and 50th quantiles exclusively represented temperatures experienced during El Niño-induced warming events (temperatures ≥ 24.8°C). The temperatures encompassed by the 48th quantile, in comparison, predominately reflected mild ENSO-related temperature excursions (such as the 2002/03 and 2009/10 El Niños) but also included some exceptionally warm “normal” months. Secondly, the variability observed in the coldest quantiles was likely an artefact produced by the model rather than a true reflection of changing environmental conditions. TAO observational data clearly demonstrate that substantial warming anomalies characterized the onset of El Niño events in the EEP subsurface, yet there is no analogous cooling related to La Niña events. The method in which the model symmetrically modulates ENSO amplitude is likely introducing an artificial cooling during La Niña months that would not occur in the natural environment. For these reasons, I based my interpretation of the Q-Q sensitivity results (as well as the Q-Q analyses of the IFA datasets) on the relative differences in the three warmest quantiles.

Model results suggest that Q-Q analyses possessed a lower threshold of detection and, therefore, were more sensitive to changes in ENSO amplitude compared with the BSD method. The warmest (50th) quantile is the most responsive to changes in ENSO, though the relative sensitivity in detecting reduced and enhanced ENSO amplitude was asymmetric (Figure 7a). In the 20% dampened scenario, the warmest quantile deviated significantly (with 90% confidence) from the mean-adjusted 1:1 line in a majority (66%) of the 10,000 Monte Carlo realizations. A 30% reduction in ENSO amplitude was detected in the warmest quantile 90% of the time. Beyond the 30% dampened ENSO scenario, the warmest quantile reported significantly reduced ENSO amplitude in nearly all (99.99%) realizations. This is in contrast to the amplified ENSO scenarios, where even a doubling of ENSO amplitude registered in the warmest quantile only 57% of the time. It is important to note that when comparing pseudo-IFA datasets sampled from the non-adjusted ENSO scenario (i.e. comparing datasets randomly sampled from the same population distribution), the warmest quantile reports a spuriously significant reduction in the warmest quantile in 27% of Monte Carlo realizations. The 49th quantile, in comparison, is slightly less sensitive than the 50th (Figure 7b). The threshold at which the 49th quantile reported significantly reduced results ~100% of the time was at 70% dampened ENSO amplitude as opposed to 40% for the 50th, though it deviated from the mean-adjusted 1:1 line in a majority (~62%) of realizations at a 40% reduction. Sensitivity of the 49th quantile in the amplified ENSO spectrum is similar to the 50th quantile, only producing a significantly positive result 57% of the time in the 100% amplified ENSO scenario. The asymmetry in quantile sensitivity is exacerbated in the case of the 48th quantile (Figure 7c). While the response to reductions in ENSO are similar to the 49th quantile, successful detection of doubled ENSO amplitude only occurred in approximately a third (34%) of Monte Carlo realizations.

4.3 Biweight Estimates of Individual Foraminifera Data

Inferred temperatures from the individual foraminifera data are shown alongside their respective histograms in Figure 8, and a summary of the computed means and BSDs for each individual time slice are presented in Table 1. Overall, the compilation of IFA Mg/Ca data range from 0.47 to 2.12 mmol/mol, corresponding to a subsurface temperature range between 10.2 and 29.0°C. One-sample Kolmogorov-Smirnov tests suggest the distributions of each time slice were not normally distributed ($p > 0.05$ in all cases). Indications of bimodality, which could result from mixing of individuals via bioturbation or sampling intervals which represent periods of climate transition, are not apparent in either of the time slices. In some cases, notably for the YD and HS1, kernel density functions illustrate some minor degree of positive skew in the paleotemperature distribution.

Notwithstanding these small differences in distributional shape, biweight estimates of spread for each time slice were remarkably constant (Table 1). BSDs exhibited a total range between 2.73 and 2.95°C over the entire period of investigation, with the YD and Modern/LH possessing the lowest and highest BSD estimates, respectively. Results from the two-sample Kolmogorov-Smirnov test suggest that significant differences existed at the 95% confidence level between some of the down-core IFA populations (Table 3). The Modern/LH population is significantly different from a number of down-core time slices (MH, HS1, and LGM), but not others (EH, YD, and BA). In contrast, Kolmogorov-Smirnov test results suggest the EH and LGM populations were significantly different from all other time slices, with the exception being between EH and Modern/LH. The two-sample Kolmogorov-Smirnov test, however, is sensitive to differences in both location and scale. To test whether the observed significant differences were the result of relative differences in the mean or in the spread of the paleotemperature distributions, I turned to the results of the Brown-Forsythe tests for equality of variance (Table 4). The results suggested no significant differences in the temperature spread of the sampled time slices, indicating that the significant differences revealed by the Kolmogorov-Smirnov tests lie primarily in the mean.

4.4 Quantile-Quantile Analyses

Before comparing the quantiles of the IFA distributions against one another, I assessed the extent to which the 09MC core-top population was representative of modern hydrographic variability by conducting a Q-Q analysis between the Modern/LH paleotemperature distribution and the distribution of TAO temperature observations from 40 m water depth. The results suggest that the distributions are identical at the 90% confidence limit, illustrated by the close proximity of the plotted quantiles to the 1:1 line (solid line) (Figure 9). This finding is consistent with IFA core-top comparisons made in other ENSO-sensitive regions of the Pacific Ocean (Rongstad et al., 2018; White et al., 2017) and provides compelling evidence that (1) IFA populations are faithful recorders of upper ocean hydrographic variability, and (2) the effects of habitat migration or seasonal variability in *N. dutertrei* abundance on the shape of paleotemperature distributions are minimal. The close correspondence between the distributional shape of the Modern/LH time slice and TAO observations justifies the use of the core-top population as a representative sample of "modern" hydrographic variability in the ensuing discussion.

With my working assumption confirmed, I applied the Q-Q method to the down-core time slices to see how paleotemperature distributions across the last deglaciation compare to the core-top. As outlined in Section 4.2, I only report on the relative differences in the warmest quantiles given their outsized representation of ENSO-related temperature anomalies. The results show that each of the Q-Q analyses exhibit a reduction of the warmest quantile when compared to the Modern/LH time slice, suggestive of a reduction in ENSO-related warming anomalies relative to today (Figures 10 and 11 for the Holocene and deglaciation/LGM, respectively). This is especially true with regards to the YD, which displays a significant reduction in all three of the warmest quantiles.

The results seem to withstand scrutiny when considering the relative effects of Q-Q detection sensitivity and IFA sampling uncertainty. Despite the tendency for the warmest quantile to generate spuriously significant results without an underlying change in hydrographic variability (a 27% chance according to the sensitivity model output), the likelihood of generating the observed results by chance is very low. Under the null hypothesis that the time slices are randomly sampled from homoscedastic population distributions (i.e. sampled from an underlying climate signal whose variability is unchanged with time), the compounded probability that I would observe a reduction in the warmest quantile for all six Q-Q comparisons is $(27\%)^6 = 0.04\%$. Interestingly, the reduction of the warmest quantiles seems to be primarily driven by the presence of two exceptionally warm individual *N. dutertrei* in the Modern/LH population, generating an extended warm tail in its associated probability density function (Figure 8). To test whether these individuals are "outliers" or a genuine representation of the underlying climate signal, I compare the Modern/LH distribution to a second distribution from the core-top of 09MC that was independently sampled, cleaned, and analyzed (Hertzberg et al., in prep). Q-Q analysis reveals that the two populations possess a strong degree of similarity (Figure 12). The extended warm tail is reproduced in the second IFA population and is statistically identical in distributional shape (with 90% confidence) to the original Modern/LH population. In short, the reduction of the warmest quantiles in the down-core populations (relative to the core-top) is a robust feature of the 17JC IFA record, with important implications regarding ENSO variability.

Unlike the inter-population comparisons I conducted when performing the Kolmogorov-Smirnov and Brown-Forsythe tests, I did not carry out multiple Q-Q analyses using other reference distributions (rather than the Modern/LH) due to concerns surrounding Q-Q detection sensitivity. Given the non-trivial probability that the Q-Q method could produce a spurious reduction in the warmest quantile, multiple comparisons among the sampled time slices could increase the likelihood of encountering one of these statistical outcomes and committing a Type 1 error. Additional information, such as an independently reproduced population distribution, would be required to confirm whether any observed differences represented a robust finding, as demonstrated above in the case of the Modern/LH time slice. Unfortunately, a full duplication of each time slice is beyond the scope of this project. Therefore, in the ensuing discussion on paleo-ENSO dynamics, I primarily focus on differences in distributional shape relative to hydrographic variability recorded in the core-top, with the acknowledgement that additional IFA populations could provide greater insight into relative differences among the down-core time slices.

5. Discussion

5.1 Implications of Statistical Treatment on ENSO Interpretation

The results from two independent statistical analyses of the individual foraminifera data offer contrasting accounts of ENSO behavior over the last 25 kyrs. The lack of significant differences between each of the BSD estimates implies that ENSO intensity was invariant across the last deglaciation, despite observed changes in the mean state (Table 4). In contrast, the Q-Q analyses demonstrate that Modern/LH ENSO variability is greater than at any other point in the last 25 kyrs (Figures 10 and 11). Although these statistical results seem to be in conflict, the results of my bootstrap sensitivity algorithm indicate that they can be reconciled with reference to the different detection sensitivities (and related uncertainties) of my applied statistical methods.

According to the model output, the heightened sensitivity of the Q-Q method is more likely to detect incremental changes in ENSO activity that could be obscured amidst the uncertainty of the BSD method (Figures 6 and 7). This is likely because the inherent resistance of the BSD method to the presence of outliers desensitizes it to small variations in the warm tail of paleotemperature distributions, where ENSO changes would primarily be manifested. Instead, the BSD estimates are slightly biased towards the center of the paleotemperature distributions, which Q-Q analyses suggest are statistically indistinguishable from one another in distributional shape (Figures 10 and 11). This could potentially explain the general consistency between the observed BSD estimates of our sampled time slices (Table 1) as well as the consistency noted in BSD estimates from a previous IFA-based paleo-ENSO study in the western tropical Pacific (Khider et al., 2011). In any case, the bias within the BSD method is likely responsible for its relatively high detection threshold and, hence, its inefficiency for paleo-ENSO reconstructions, at least within the EEP.

The difference in detection sensitivities between the BSD and Q-Q methods offers a useful constraint on the magnitude of paleo-ENSO variability exhibited within the IFA record. Provided that Q-Q analyses detect significant reductions in ENSO variability that the biweight estimates do not, we can conclude that ENSO activity throughout the last 25 kyrs was indeed reduced relative to today, although the magnitude of these reductions likely never exceeded 50%. This estimate is consistent with other proxy reconstructions and modeling studies that have attempted to characterize the magnitude of paleo-ENSO amplitude change within the Holocene and LGM, which typically range from 15 – 50% (Koutavas et al., 2006; Koutavas and Joanides, 2012; Sadekov et al., 2013; Emile-Geay et al., 2016; Zheng et al., 2008; Liu et al., 2014). For the first time, however, the IFA data from 17JC are able to place an upper constraint on the magnitude of ENSO variability during the millennial-scale climate events of the last deglaciation.

It is important to note that without estimates of sampling uncertainty and detection sensitivity, there would be no objective method for identifying which of the results (the BSD estimates or the Q-Q comparisons) provided a more reliable record of paleo-ENSO activity. By extension, any implications regarding paleo-ENSO dynamics would be entirely dependent upon which statistical tool was employed. I therefore strongly recommend that future IFA-based studies incorporate some degree of sensitivity and uncertainty quantification into their experimental design in order to ensure that their conclusions are based on the most appropriate statistical methodology. Although my sensitivity analysis has its limitations (i.e. the brevity and location of the observational time series, the method by which the ENSO frequency band was extracted and modulated, the limited number of statistical methods tested, etc.), the output remains invaluable for contextualizing my seemingly contrasting results. In the same way, prefacing IFA-based reconstructions with careful and reasoned considerations on how ENSO changes are translated into IFA-statistical space (and the uncertainties associated with such a translation) may help resolve one potential source of discrepancy among IFA-based studies. Therefore, given the results of the sensitivity model, I solely focus on the results of the Q-Q analyses in my interpretation of paleo-ENSO activity over the last 25 kyrs.

5.2 The Holocene

Q-Q analyses of the Holocene time slices against the Modern/LH reveal a reduction in early and mid-Holocene ENSO activity (Figure 10). This trend of Holocene ENSO variability is qualitatively consistent with paleo-ENSO reconstructions which suggest a gradual increase in ENSO activity from the early to late Holocene (Tudhope et al., 2001; Leduc et al., 2009b; White et al., 2017; Rodbell et al., 1999; Moy et al., 2002; Conroy et al., 2008), yet differs from other records which show a mid-Holocene minimum in ENSO amplitude relative to the rest of the Holocene (McGregor and Gagan; 2004; Koutavas et al., 2006; Koutavas and Joanides, 2012; Carré et al., 2014; Emile-Geay et al., 2016; Chen et al., 2016). Notably, a gradual intensification of ENSO across the Holocene has been consistently reproduced by climate model simulations (Clement et al., 1999, 2000; Liu et al., 2000, 2014; Otto-Bliesner et al., 2003; Braconnot et al., 2012; Salau et al., 2012) which have largely been unsuccessful in replicating the mid-Holocene minimum exhibited by other proxy records (Lu et al., 2018).

To better understand what role background climate conditions may have played in producing this Holocene trend, we combine our record of EEP subsurface hydrography with a number of previously published proxy records which represent various components of the tropical Pacific mean state (Figure 13). A number of mechanisms have been proposed to explain the reduction in ENSO variability during the early to mid-Holocene, most of which invoke changes in air-sea interactions in response to variations in solar insolation forcing driven by Earth's precession (Lu et al., 2018). One such mechanism, the ocean dynamical thermostat, emphasizes the influence of the seasonal contrast in equatorial insolation (March minus September) on tropical Pacific surface hydrography and its subsequent impact on tropical atmospheric circulation (Clement et al., 2000). Model simulations demonstrate that when equatorial insolation is at its peak during late boreal summer (when El Niño events tend to develop rapidly), an asymmetric heating response between the east and west Pacific enhances the zonal Pacific SST gradient and, in turn, strengthens the Walker circulation (Clement et al., 1996, 2000; Luo et al., 2017). A stronger Walker circulation increases trade wind strength over the EEP and enhances upwelling in the cold tongue, which in turn further exacerbates the zonal SST gradient and reinforces the initial increase in trade wind strength through the positive Bjerknes feedback (Bjerknes, 1969). As a result, the mean climatology of the tropical Pacific resembles a La Niña-like configuration in which the increased surface wind stress acts as a barrier against the eastward propagation of warm SST anomalies from the west Pacific (Clement et al., 2000). Overall, this collective state of the tropical Pacific ocean-atmosphere system inhibits the development of El Niño events and reduces ENSO variability on broader time scales (Clement et al., 2000; Koutavas and Joanides, 2012; Sadekov et al., 2013).

Our proxy data compilation demonstrates that La Niña-like mean state conditions prevailed during the mid-Holocene (Figure 13). Between ~4 – 6 kyrs, when late summer equatorial insolation was at a maximum, EEP subsurface temperatures were generally cooler (this study; Pena et al., 2008; Sadekov et al., 2013) and the zonal SST gradient was enhanced (Koutavas and Joanides, 2012; Sadekov et al., 2013), suggest an orbitally-driven initiation of La Niña-like mean state conditions. This is corroborated by speleothem records of monsoonal rainfall from caves in southeast China, where stronger monsoon conditions during the mid-Holocene are consistent with a strengthening of the Walker circulation (Yuan et al., 2004). These observations have largely been invoked to explain the prominent mid-Holocene minimum found in some reconstructions of paleo-ENSO variability (Koutavas et al., 2006; Koutavas and Joanides, 2012) but on its own cannot sufficiently explain the trends observed in our IFA dataset, particularly during the early Holocene. Assuming changes in ENSO variability are a simple, linear response to the strength of the zonal SST gradient as posited by Koutavas and Joanides (2012) and Sadekov et al. (2013), the similar estimates in the magnitude of the zonal SST contrast during the EH and Modern/LH would imply comparable degrees of ENSO activity at these times (Figure 13). This runs counter to our observations which indicate a relative reduction in EH ENSO compared to the Modern/LH time slice.

The inconsistency between the predictions of the ocean dynamical thermostat and the outcomes of our IFA data argues against the idea that one dynamic coupling (in this case the link between sea surface hydrography and atmospheric circulation) holds a consistent influence over ENSO variability throughout the Holocene. Theoretical work and model simulations strongly suggest that ENSO is modulated by a complex network of amplifying and dampening feedbacks, modified in strength and influence based on changes in background climate conditions (Liu et al., 2014; Lu et al., 2018). It is likely that the influence of the ocean dynamical thermostat was diminished by changes in the strength of other dynamic feedbacks which held greater sway over the evolution of Holocene ENSO activity.

One such possibility is a reduction in the strength of the positive upwelling feedback, caused by a warming of the equatorial thermocline driven remotely by southern hemisphere insolation changes (Liu et al., 2000, 2014; White et al., 2017). EEP thermocline waters, which are primarily sourced from the south Pacific surface ocean, are sensitive to changes in southern hemisphere subtropical SSTs (Hanawa and Talley, 2001; Johnson and McPhaden, 1999; Liu et al., 2003; Fielder and Talley, 2006). During boreal summer (or austral winter; JJA), the increase in solar insolation warms the south Pacific surface ocean, and the greater wintertime mixing subsequently subducts these waters beneath the surface (Hanawa and Talley, 2001). The newlygenerated subtropical mode waters are then transmitted to the EEP subsurface through an interior circulation pathway set up by shallow meridional circulation cells, which move mode waters equatorward, and the EUC, which transports them towards the eastern Pacific margin (Johnson and McPhaden, 1999; Hanawa and Talley, 2001; O'Connor et al., 2002; Nie et al., 2019; Fielder and Talley, 2006). Once advected to the EEP, the warmer subsurface waters erode the regional thermocline and reduce upper ocean thermal stratification within the EEP. In effect, a warmer subsurface desensitizes the surface ocean response to trade wind anomalies by damping the impact of upwelled waters on zonal SST patterns (Dijkstra, 2006; Liu et al., 2000, 2014; White et al., 2017). This reduction in coupling strength between the trade winds and tropical Pacific SSTs undercuts the foundation of the Bjerknes feedback, a critical dynamic coupling for ENSO development, and consequently stabilizes long-term ENSO variability (Liu et al., 2000, 2014; Lu et al., 2018).

Following this mechanism, the gradual decrease in austral winter insolation across the Holocene could potentially explain the trend in ENSO variability depicted by our IFA data (Figure 13). Austral winter insolation peaks during the early Holocene (~10 kyrs) and progressively decreases into the modern, which would be consistent with our observed reduction in EH and MH ENSO relative to the Modern/LH. Moreover, the mechanism is supported by a series of transient climate model simulations which, through a technique known as Bjerknes stability analysis (Jin et al., 2006; Kim and Jin, 2011), simulate a gradual intensification in the strength of the upwelling feedback from the early Holocene to the present (as well as other key positive ENSO modulating feedbacks, although to a lesser extent) (Liu et al., 2014).

A compilation of EEP subsurface temperature records, including the multi-shell record presented in this study, indicate a moderate warming during the early Holocene at a time when southern midlatitude insolation was at a peak (Pena et al., 2008; Sadekov et al., 2013) (Figure 13). However, the timing and magnitude of this warming differs among records, which may ostensibly be due to differences in foraminiferal test size, core location (e.g. east vs. west of the Galápagos archipelago), and sample cleaning procedure used in the various records. Unfortunately, no records from the thermocline source region exist that might help reconcile these small discrepancies (White et al., 2017). The nearest SST record, located along the Peru Margin at ~30°S, reports a peak in SSTs during the early Holocene which seemingly lends support to the thermocline warming mechanism (Kaiser et al., 2008), yet the pacing of this warming differs from the EEP records. Moreover, two of the three subsurface records (this study; Pena et al., 2008) show a warming during the late Holocene that, according to the proposed mechanism, would lead to reduction in ENSO amplitude, a prediction not supported by our IFA data (Figure 13c). Altogether, the inconsistency among EEP subsurface temperature records and a lack of records from mode water source regions make it difficult to unequivocally determine whether (and to what extent) the thermocline warming mechanism is responsible for Holocene ENSO modulation. Nevertheless, the qualitative consistency between the predictions of the mechanism and the trends exhibited by the compilation of proxy and IFA data make it a likely candidate. More records, specifically from the EEP subsurface and subtropical South Pacific, are required to validate this hypothesis.

5.3 The Last Glacial Maximum

The 17JC IFA record suggests that the LGM was characterized by reduced ENSO variability relative to the Modern/LH (Figure 11d). Our findings corroborate some previous studies that also find a reduction in ENSO during the LGM (Ford et al., 2015; Leduc et al., 2009b; Tudhope et al., 2001) but contradict others which find that LGM ENSO was enhanced

(Koutavas and Joanides, 2012; Sadekov et al., 2013). The latter group of studies have attempted to characterize ENSO behavior by extending the predictions of the ocean dynamical thermostat to glacial climate conditions. The zonal SST gradient is estimated to have been weaker during the LGM (Figure 13d), which would have led to a reduction in Walker circulation strength (Koutavas and Joanides, 2012; Sadekov et al., 2013). Under this El Niño-like mean state configuration, the weaker Walker circulation (and, consequently, the reduced wind stress) would have generated conditions more conducive to enhanced ENSO variability by allowing warm waters to propagate eastward more easily.

Nevertheless, concerns about the methods and statistical approach used by Koutavas and Joanides (2012) and Sadekov et al. (2013) have led to doubts surrounding the veracity of their conclusions (Ford et al., 2015). For example, Koutavas and Joanides (2012) rely upon estimates of ENSO variability derived from parametric measures of scale (specifically variance) which can easily be compromised by the presence of outlying values, leading to an overestimation of hydrographic variability (see section 3.2). In addition to this, the use of surface-dwelling foraminifera by Koutavas and Joanides (2012) to estimate ENSO variability has been a particularly strong point of criticism considering that SST variability in the EEP surface ocean is primarily governed by the seasonal cycle (Thirumalai et al., 2013; Fiedler and Talley, 2006). Results from a recent IFA sensitivity analysis (Thirumalai et al., 2013), as well as a reanalysis of the Koutavas and Joanides (2012) data using more robust statistical tools (Ford et al., 2015), strongly suggest that IFA populations of surface-dwelling foraminifera likely do not reflect changes in interannual, ENSO-related variability, but instead predominately record changes in the amplitude of the annual cycle. Ford et al. (2015) suggest that the IFA populations of Koutavas and Joanides (2012) provide evidence for stronger seasonality during the LGM rather than an increase in ENSO activity. Such an observation is not in direct conflict with my results. Indeed, a collection of modeling results suggest an inverse relationship between the strength of the annual cycle and ENSO variability (Chang et al., 1994, 1995; Liu, 2002; Liu et al., 2014; Federov and Philander, 2001). If true, then an enhanced LGM annual cycle is fully consistent with our observations of a reduced LGM ENSO.

Similarly, a number of methodological shortcomings call into question the conclusion of an enhanced LGM ENSO by Sadekov et al. (2013). Although the general approach is similar to the present study (both reconstruct subsurface temperature variability from geochemical analyses of *N. dutertrei*), differences related to individual sample size, the number of samples analyzed per time slice, and statistical processing likely contribute to the discrepancy between our respective results. First, it should be noted that the repetitive Mg/Ca analyses performed by Sadekov et al. (2013) were not on individual foraminiferal shells (like other IFA-based paleo-ENSO reconstructions), but on samples which combine 2 – 3 shells. Combining multiple specimens in a single sample averages the geochemical signature of the individual foraminifera, artificially smoothing the variability of a given time slice. The authors attempt to account for this averaging effect by back-calculating a theoretical standard deviation (as if they measured individual shells) by assuming that standard deviation follows a simple, gaussian relationship as a function of the number of shells analyzed. This computation of theoretical IFA values, rather than directly measuring individual shells, introduces an additional degree of error which could compromise their estimates of ENSO variability. Furthermore, the number of samples analyzed per time slice by Sadekov et al. (2013) (n = 24) is likely insufficient to fully characterize EEP subsurface hydrographic variability. Smaller population sizes are associated with larger uncertainties in their estimates of hydrographic variability (Thirumalai et al., 2013), and thus

Sadekov et al. (2013) might be generating a false positive signal and overestimating LGM ENSO activity. Finally, Sadekov et al. (2013) estimate variability based on distributions of measured Mg/Ca ratios and not calibrated Mg/Ca paleotemperatures. Nonlinearity in proxy-parameter relationships, like between foraminiferal Mg/Ca and ocean temperature, can lead to exaggerated estimates of paleoenvironmental variability when not properly accounted for (Emile-Geay and Tingley, 2016). In short, we argue that the paleo-ENSO studies which report an enhanced LGM ENSO (Koutavas and Joanides, 2012; Sadekov et al., 2013) have some non-trivial methodological shortcomings that could bias their conclusions regarding ENSO variability. Having accounted for these variables in the design of our study, we believe our observation of a reduced LGM ENSO offers a more tenable accounting of glacial-interglacial ENSO evolution.

Evidence from proxy reconstructions and model simulations attributes this reduced glacial ENSO state to changes in EEP subsurface hydrography, most notably a deeper mean thermocline (Ford et al., 2015, 2018; Zhu et al., 2017; Federov and Philander, 2001). Theoretical work has hypothesized that there are two distinct “modes” of ENSO variability, distinguishable by their emphasis on different dynamic feedbacks which determine ENSO behavior (Federov and Philander, 2001; Guilyardi et al., 2009). First, an “SST mode” modulates ENSO primarily through the impact of trade wind-induced upwelling on the zonal SST gradient (Federov and Philander, 2001). This mode is most favored when the EEP thermocline is shallow and the overall ocean dynamic response to a given trade wind anomaly is increased. A shallower thermocline places colder sub-thermocline waters closer to the surface, where they are more likely to be upwelled by the trade winds and contribute to the development of the zonal SST gradient (Dijkstra, 2006). This enhances the surface ocean’s sensitivity to trade wind perturbations and bolsters the coupling strength of the Bjerknes feedback, leading to a more variable ENSO. When the mean depth of the EEP thermocline is deeper, the ENSO system toggles from the "SST mode" to a "thermocline mode" which reduces ENSO variability by diminishing the coupling strength of positive ENSO modulating feedbacks (Federov and Philander, 2001). A deeper EEP thermocline increases subsurface temperature at the level of upwelling, and so the relatively warmer waters being upwelled have a smaller influence over SST patterns (similar to the thermocline warming mechanism detailed in section 5.2) (Dijkstra, 2006). A deeper thermocline is also less perturbed by variations in trade wind strength, which acts to maintain a mode of overall reduced ENSO variability (Dijkstra, 2006).

This theory of glacial-interglacial ENSO modulation is supported by paleoenvironmental records (Ford et al., 2015, 2018; Spero et al., 2003; Patrick and Thunell, 1997; Faul et al., 2000) and model simulations (Zhu et al., 2017). Reconstructions of EEP upper ocean density structure using stable oxygen and carbon isotopes have indicated that the EEP thermocline was indeed deeper than today (Spero et al., 2003; Ford et al., 2018). This is likely a response to a more southerly mean position of the ITCZ, as indicated by a sediment reflectance record from the Cariaco Basin (Peterson et al., 2000; Figure 13e). A southerly-displaced ITCZ would reduce the cross-equatorial flow of the trade winds at the core location, which would lead to a reduction in mean upwelling intensity and, consequently, suppress the EEP thermocline.

It is difficult, however, to determine whether the down-core subsurface temperature record from 17JC supports a "thermocline mode" of ENSO variability. The 17JC multi-shell Mg/Ca record suggests EEP subsurface temperatures were on average 3.2°C cooler during the LGM, approximately double the magnitude of regional cooling in the EEP surface ocean (1.6°C; Ford et al., 2015). Although cooler glacial SSTs are consistent with weaker radiative forcing associated with lower atmospheric CO_2 concentrations (Bereiter et al., 2015; Figure 13f), the cause of the larger and more abrupt cooling in the EEP subsurface is less clear. One possibility is that a greater surface ocean cooling in the southern hemisphere midlatitudes was transmitted to the EEP subsurface via the interior circulation pathway connecting the subtropical south Pacific and the equatorial Pacific. This would lead to an increase in the EEP vertical temperature gradient (i.e. a sharper thermocline), which, combined with a deeper thermocline, would have a stabilizing effect over ENSO variability (Federov and Philander, 2001). Unfortunately, the subtropical south Pacific is a sparsely sampled region of the global ocean, and little is known about its thermal history (MARGO Project Members, 2009). The nearby SST record from the Peru Margin (Kaiser et al., 2008) suggests a moderate glacial cooling of ~2°C, not enough to account for the full magnitude of the EEP subsurface cooling. Moreover, reconstructed stable oxygen and carbon isotopic gradients from the EEP suggest a reduction in upper ocean stratification, not an enhancement (Spero et al., 2003; Ford et al., 2018), and would therefore argue against the reasoning above.

If the stable oxygen and carbon isotope gradients are correct and the EEP thermocline was indeed deeper and weaker than today, the reduction of the vertical temperature gradient could have altered upper ocean density stratification and shifted the mean position of the deep chlorophyll maximum layer with respect to the depth of the thermocline. This could have shifted the mean calcification depth of *N. dutertrei* from a generally mid-thermocline position to a slightly deeper habitat in the lower thermocline. The greater cooling exhibited in our 17JC subsurface temperature record, therefore, could be explained by a combination of glacial cooling (1.6°C) and an additional cooling related to a population-wide shift to a deeper depth habitat. A weaker vertical temperature gradient, although capable of explaining the cooling in our multi-shell subsurface temperature record, would have some implications in the interpretation of our

IFA results for the LGM. Each of our IFA paleotemperature distributions integrate a degree of variability that can be attributed to intraspecific differences in calcification depth (Thirumalai et al., 2013; Sadekov et al., 2013). If the EEP thermocline was weaker than today, the spread of ocean temperatures contained within the depth window of *N. dutertrei* would decrease and could, in effect, reduce the variability recorded within the population of individual foraminifera. The competing effects of a reduction in ENSO variability (due to a deeper EEP thermocline) and a reduced vertical temperature gradient on the shape of the LGM paleotemperature distribution are hard to parse without reconstructions of EEP density stratification using rigorous Monte Carlo-based methods (Ford et al., 2018), a task which goes beyond the present study.

It should be noted, however, that other subsurface temperature records from the region do not record as large (or as abrupt) a glacial subsurface cooling as 17JC, and instead show a cooling similar in pacing and magnitude to the surface ocean (Figure 13c; Pena et al., 2008; Sadekov et al., 2013). The inconsistencies among these records underscore the need for more high-resolution records from the EEP subsurface and the thermocline water source region in the south Pacific. Although the cause of the subsurface cooling during the LGM is largely unknown, the compilation of proxy data and the results of our Q-Q analyses support the notion that adjustments in EEP upper ocean stratification likely had a damping effect on LGM ENSO amplitude.

5.4 The Last Deglaciation

The 17JC IFA results indicate a generally reduced ENSO state (relative to Modern/LH) across the abrupt climate events of last deglaciation (Figure 11a – c). Initially, this would seem to suggest that ENSO was invariant, maintaining a relatively stable yet reduced state despite millennial-scale oscillations in background climate conditions. However, small differences among the deglacial Q-Q analyses could be indicative of subtle changes in ENSO activity related to millennial-scale climate change, particularly in the case of the YD. The YD is the only time slice among those sampled to exhibit a significant reduction in all three of the warmest quantiles (Figure 11a). These results could plausibly be interpreted as a greater reduction in ENSO amplitude during the YD in comparison to the other time slices spanning the last 25 kyrs.

Given the paucity of paleo-ENSO records spanning the deglacial period, few results lend themselves to direct comparison with our own. The most comparable record is that of Sadekov et al. (2013), which, like the present study, estimates paleo-ENSO activity by reconstructing subsurface temperature variability using *N. dutertrei* from multiple time slices across the deglacial period. The authors report generally enhanced deglacial ENSO activity relative to the Holocene, in contrast to the results from 17JC. However, given the concerns detailed in section 5.3, it is likely that the methods employed by Sadekov et al. (2013) lead to an overestimation in hydrographic variability that could bias their conclusions regarding deglacial ENSO variability. Additionally, time slices from two other IFA-based paleo-ENSO studies have each reported a single “snapshot” of ENSO variability during the deglacial period (Leduc et al., 2009b; White et al., 2017). A comparison of these IFA populations (one from HS1 and one from the YD) with time slices from the late Holocene reveal no statistically significant differences in ENSO activity, in conflict with the interpretation of both the 17JC results and those of Sadekov et al. (2013).

In the absence of a more unambiguous paleoenvironmental record of deglacial ENSO variability, high-resolution climate model simulations can provide further insight into the environmental controls likely responsible for deglacial ENSO modulation (Liu et al., 2014; Lu et al., 2016). Across the last deglaciation, a number of critical components of the background climate state were in a period of flux: CO_2 concentrations were rising (Petit et al., 1999; Bereiter et al., 2015), continental ice sheets were retreating (Carlson et al., 2008; Bentley et al., 2010), and circulation patterns within the interior ocean and overlying atmosphere underwent significant changes in configuration and strength (McManus et al., 2004; Schmidt et al., 2012b; Rühlemann et al., 1999; Koutavas and Lynch-Stieglitz, 2004; Them et al., 2015; Broccoli et al., 2006). Transient model simulations demonstrate that the net influence of these mean state components produce millennial-scale trends in simulated ENSO variability superimposed upon the larger, more gradual trend related to the dominating influence of orbital forcing (Liu et al., 2014). Other modelling studies provide greater context by revealing that, in isolation, individual components of the background climate state modulate ENSO in various ways and often in opposing directions (Timmerman et al., 2007a, b; Merkel et al., 2010; Braconnot et al., 2012; Liu et al., 2014; Lu et al., 2016; Williamson et al., 2018).

According to model simulations, one component of potential importance is the influence of North Atlantic meltwater events on ITCZ variability in the Pacific. Evidence from water-hosing experiments designed to test the influence of meltwater forcing over global climate patterns (Timmerman et al., 2007a, b; Liu et al., 2014; Lu et al., 2016; Williamson et al., 2018) suggest that variability in the mean position of the ITCZ could have played a critical role in deglacial ENSO modulation. In these simulations, input of freshwater into the North Atlantic leads to a shutdown of the Atlantic Meridional Overturning Circulation (AMOC). As a crucial redistributor of heat among the northern and southern hemispheres in the Atlantic basin, a shutdown in the AMOC allows heat to build up in the South Atlantic, forcing the ITCZ to shift southward. These reconfigurations in oceanic and atmospheric circulation lead to a relative increase in ENSO variability in a majority of model outputs (Timmerman et al., 2007a, b; Braconnot et al., 2012; Liu et al., 2014; Lu et al., 2016; Williamson et al., 2018). In one model which integrates multiple external forcing mechanisms in their simulation of ENSO, the influence of the AMOC and ITCZ is second only to Earth's precession cycle (Liu et al., 2014).

The mechanism invoked to explain this causal relationship relates to the amplitude of the equatorial annual cycle. During periods of reduced AMOC, the southward displacement of the ITCZ generates a more symmetric meridional SST gradient between the EEP cold tongue and the east Pacific warm pool to the north, reducing seasonality at the equator. The opposite holds true for interstadial events such as the BA, where a resumption of AMOC and a northward displacement of the ITCZ enhances the meridional SST gradient and increases seasonality. In response, the ENSO is modified through the non-linear mechanism of frequency entrainment (Chang et al., 1994, 1995; Liu, 2002). In short, when the annual cycle is sufficiently strong, the ENSO is capable of "relinquishing" its natural oscillatory mode to acquire the frequency of the annual cycle. This has the effect of substantially weakening interannual climate variability and ENSO amplitude (Chang et al., 1994, 1995; Liu, 2002). When seasonality is reduced during periods of weakened AMOC, the decreased damping effect from the annual cycle leads to a relative increase in ENSO amplitude (Timmerman et al., 2007a, b; Liu, 2002; Williamson et al., 2018).

There is substantial paleoceanographic evidence to suggest that variations in the AMOC (Lynch-Stieglitz et al., 1999a; McManus et al., 2004; Came et al., 2008; Ritz et al., 2013; Valley et al., 2017) and the latitudinal position of the ITCZ (Peterson et al., 2000; Schmidt et al., 2004; Broccoli et al., 2006; Schmidt and Lynch-Stieglitz, 2011; Schmidt et al., 2012b; Reimi and Marcantonio, 2016; Loveley et al., 2017) characterized the deglacial period. Following the predictions of the frequency entrainment mechanism, one could expect enhanced ENSO variability during the YD and HS1 and dampened ENSO during the BA. These predictions are not wholly consistent with the 17JC IFA record (Figure 11b). Q-Q analyses indicate an ENSO reduction in BA ENSO, which conforms to the predictions of the frequency entrainment mechanism. However, our results also indicate a reduction in ENSO during HS1 and the YD, suggesting that the influence of the ITCZ position was likely not the only forcing mechanism modifying ENSO behavior across the last deglaciation.

Other components of the background climate state could be regulating ENSO variability in competition with the influence of the ITCZ. For example, the multi-shell Mg/Ca and IVF-$\delta^{18}O_{SW}$ records from 17JC suggest that the EEP subsurface underwent significant hydrographic changes during deglacial climate events (Figure 5). The coherent trends in subsurface temperature and salinity suggest that they reflect EEP thermocline migrations in response to changes in the mean position of the ITCZ (Peterson et al., 2000). During stadial events, a warmer and saltier subsurface suggests a deeper EEP thermocline. This change in upper ocean thermal stratification could have weakened the coupling strength of critical air-sea feedback processes important for modulating ENSO. This would have had the net effect of decreasing ENSO variability, potentially counterbalancing the amplifying influence of the frequency entrainment mechanism. Other features of deglacial climate, such as rising CO_2 concentrations (Bereiter et al., 2014), could have also influenced ENSO amplitude. However, model experiments generally disagree on the net effect changes in atmospheric CO_2 has on ENSO amplitude (Liu et al., 2014; Zhu et al., 2017; Collins et al., 2010; Latif and Keenlyside, 2009; Meehl et al., 2006; Timmerman et al., 2004).

In short, the environmental controls over ENSO variability in the deglacial period remain uncertain and require further study. The feedback processes responsible for deglacial ENSO modulation were likely multi-faceted, with various components of background climate forcing

ENSO in different directions and to varying degrees. Although further work is required to help clarify the relative roles of these individual feedbacks over deglacial ENSO modulation, our results clearly suggest a general reduction in deglacial ENSO relative to the Modern/LH.

6. Conclusions

In this study, I presented a new high-resolution record of paleo-ENSO variability spanning the last 25 kyrs by reconstructing EEP subsurface temperature variability using a Mg/Ca-based IFA approach on a high sedimentation rate piston core, 17JC, and its corresponding multi-core, 09MC. The close correspondence between EEP subsurface temperature variability in modern observations and the variability recorded by individual subsurface-dwelling foraminifera in core-top sediments suggests that IFA is a powerful tool for reconstructing past changes in paleo-ENSO activity. The IFA datasets presented here are the first to use Mg/Ca-paleotemperature estimates to resolve the millennial-scale climate oscillations of the last deglaciation, filling key gaps in our knowledge of ENSO history and its response to rapid climate change.

IFA populations from the early to mid-Holocene, the LGM, and the abrupt climate events of the last deglaciation all exhibit a reduction in ENSO variability relative to the core-top. Based upon the results of a bootstrap Monte Carlo sensitivity analysis, the reduction in past ENSO variability is estimated to be no greater than 50% of the variability exhibited by the core-top. An explanation for this largely dampened ENSO state relies heavily on the notion that ENSO modulating feedbacks are dynamic and modified in relative strength and influence as a function of changing background climate conditions. During the early to mid-Holocene, for example, ENSO was likely dampened by an erosion of the regional thermocline when subtropical mode waters, warmed by an increase in austral winter insolation, were advected from south Pacific midlatitudes to the EEP. Consequently, the warmer thermocline waters desensitized the surface ocean's response to trade wind anomalies, weakening the ENSO's positive upwelling feedback. During the LGM, a deeper mean EEP thermocline in response to a more southerly ITCZ moved the ENSO system into a dampened "thermocline mode" which reduced ENSO variability by weakening both the upwelling and thermocline feedbacks. Deglacial ENSO variability, in contrast, is more complex from a mechanistic standpoint. Model simulations suggest that shutdowns of the AMOC and latitudinal migrations in the ITCZ dominate millennial-scale ENSO variability through the mechanism of frequency entrainment. However, this mechanism on its own fails to explain the observed reduction in HS1 ENSO and the potentially greater reduction in ENSO during the YD. Other factors, such as changes in EEP upper ocean stratification and rising CO_2 concentrations, could have contributed to the general reduction in deglacial ENSO; however, further work is required to help clarify the relative roles of these individual feedbacks.

Although climate change over the past 25 kyrs cannot serve as a direct analog for anthropogenic warming, the results from 17JC carry important implications for future projections of ENSO variability. Current state-of-the-art climate models possess strong biases in their simulation of important air-sea interactions within the EEP (Seager et al., 2019) and these biases can lead to inaccurate representation of the amplifying and dampening feedback processes responsible for determining ENSO behavior. Improvement of model performance is critical for both more detailed investigations into the relative potency of individual ENSO modulating feedbacks (and under what conditions they flourish in) as well as how future climate change will alter these processes, and by extension ENSO development. The results from 17JC, particularly during the last deglaciation, can be used to test general coupled ocean-atmosphere models pivotal for understanding the response of the ENSO to abrupt climate change.

REFERENCES

Allen, K. A., Hönisch, B., Eggins, S. M., Haynes, L. L., Rosenthal, Y., & Yu, J. (2016). Trace element proxies for surface ocean conditions: A synthesis of culture calibrations with planktic foraminifera. *Geochimica et Cosmochimica Acta*, *193*, 197–211. https://doi.org/10.1016/j.gca.2016.08.015

An, S. Il, & Choi, J. (2014). Mid-Holocene tropical Pacific climate state, annual cycle, and ENSO in PMIP2 and PMIP3. *Climate Dynamics*, *43*(3–4), 957–970. https://doi.org/10.1007/s00382-013-1880-z

An, S. I., Timmermann, A., Bejarano, L., Jin, F. F., Justino, F., Liu, Z., & Tudhope, A. W. (2004). Modeling evidence for enhanced El Niño-Southern Oscillation amplitude during the Last Glacial Maximum. *Paleoceanography*. https://doi.org/10.1029/2004PA001020

Anand, P., Elderfield, H., & Conte, M. H. (2003). Calibration of Mg/Ca thermometry in planktonic foraminifera from a sediment trap time series. *Paleoceanography*, *18*(2), n/a-n/a. https://doi.org/10.1029/2002PA000846

Barker, S., Greaves, M., & Elderfield, H. (2003). A study of cleaning procedures used for foraminiferal Mg/Ca paleothermometry. *Geochemistry, Geophysics, Geosystems*, *4*(9). https://doi.org/10.1029/2003GC000559

Bemis, B., Spero, H. J., Bijma, J., & Lea, D. W. (1998). Reevaluation of the oxygen isotopic composition of planktonic foraminifera: Experimental results and revised paleotemperature equations. *Paleoceanography*, *13*(2), 150–160.

Bentley, M. J., Fogwill, C. J., Le Brocq, A. M., Hubbard, A. L., Sugden, D. E., Dunai, T. J., & Freeman, S. P. H. T. (2010). Deglacial history of the West Antarctic Ice Sheet in the Weddell Sea embayment: Constraints on past Ice volume change. *Geology*. https://doi.org/10.1130/G30754.1

Bereiter, B., Eggleston, S., Schmitt, J., Nehrbass-Ahles, C., Stocker, T. F., Fischer, H., et al. (2015). Revision of the EPICA Dome C CO2 record from 800 to 600-kyr before present. *Geophysical Research Letters*, *42*(2), 542–549. https://doi.org/10.1002/2014GL061957

Bjerknes, J. (1966). A possible response of the atmospheric Hadley circulation to equatorial anomalies of ocean temperature. *Tellus*, *18*(4), 820–829. https://doi.org/10.3402/tellusa.v18i4.9712

Bjerknes, J. (1969). Atmospheric Teleconnections from the Equatorial Pacific. *Monthly Weather Review*, *97*(3), 163–172. https://doi.org/10.1175/1520-0493(1969)097<0163:atftep>2.3.co;2

Blunden, J., Arndt, D. S., & Hartfield, G. (Eds.). (2018). State of the climate in 2017. *Bulletin of the American Meteorological Society*, *99*(8), Si – S332. https://doi.org/10.1175/2018BAMSStateoftheClimate.1

Braconnot, P., Luan, Y., Brewer, S., & Zheng, W. (2012). Impact of Earth's orbit and freshwater fluxes on Holocene climate mean seasonal cycle and ENSO characteristics. *Climate Dynamics*, *38*(5–6), 1081–1092. https://doi.org/10.1007/s00382-011-1029-x

Brown, J., Collins, M., Tudhope, A. W., & Toniazzo, T. (2008). Modelling mid-Holocene tropical climate and ENSO variability: Towards constraining predictions of future change with palaeo-data. *Climate Dynamics*, *30*(1), 19–36. https://doi.org/10.1007/s00382-007-0270-9

Brown, M. B., & Forsythe, A. B. (1974). Robust tests for the equality of variances. *Journal of the American Statistical Association*, *69*(346), 364-367. https://doi.org/10.1080/01621459.1974.10482955

Bush, A. B. G. (2007). Extratropical influences on the El Niño-southern oscillation through the late Quaternary. *Journal of Climate*, *20*(5), 788–800. https://doi.org/10.1175/JCLI4048.1

Cai, W., Santoso, A., Wang, G., Yeh, S. W., An, S. Il, Cobb, K. M., et al. (2015). ENSO and greenhouse warming. *Nature Climate Change*, *5*(9), 849–859. https://doi.org/10.1038/nclimate2743

Came, R. E., Oppo, D. W., Curry, W. B., & Lynch-Stieglitz, J. (2008). Deglacial variability in the surface return flow of the Atlantic meridional overturning circulation. *Paleoceanography*, *23*(1), 1–10. https://doi.org/10.1029/2007PA001450

Carré, M., Sachs, J. P., Purca, S., Schauer, A. J., Braconnot, P., Falcón, R. A., et al. (2014). Holocene history of ENSO variance and asymmetry in the eastern tropical Pacific. *Science (New York, N.Y.)*, *345*(6200), 1045–1048. https://doi.org/10.1126/science.1252220

Chang, P., Ji, L., Wang, B., & Li, T. (1995). Interactions between the Seasonal Cycle and El Niño-Southern Oscillation in an Intermediate Coupled Ocean-Atmosphere Model. *Journal of the Atmospheric Sciences*, *52*(13), 2353–2372. https://doi.org/10.1175/1520-0469(1995)052<2353:ibtsca>2.0.co;2

Chang, P., Wang, B., Li, T., & Ji, L. (1994). Interactions between the seasonal cycle and the Southern Oscillation - Frequency entrainment and chaos in a coupled ocean-atmosphere model. *Geophysical Research Letters*, *21*(25), 2817–2820. https://doi.org/10.1029/94GL02759

Chen, S., Hoffmann, S. S., Lund, D. C., Cobb, K. M., Emile-Geay, J., & Adkins, J. F. (2016). A high-resolution speleothem record of western equatorial Pacific rainfall: Implications for Holocene ENSO evolution. *Earth and Planetary Science Letters*, *442*, 61–71. https://doi.org/10.1016/j.epsl.2016.02.050

Choi, J., An, S. Il, & Yeh, S. W. (2012). Decadal amplitude modulation of two types of ENSO and its relationship with the mean state. *Climate Dynamics*, *38*(11–12), 2631–2644. https://doi.org/10.1007/s00382-011-1186-y

Clement, A. C., Seager, R., & Cane, M. A. (1999). Orbital controls on the El Nino/Southern Oscillation and the tropical climate. *Paleoceanography*, *14*(4), 441–456. https://doi.org/10.1029/1999PA900013

Clement, A. C., Seager, R., & Cane, M. A. (2000). Suppression of El Niño during the mid-Holocene by changes in the Earth's orbit. *Paleoceanography*, *15*(6), 731–737. https://doi.org/10.1029/1999PA000466

Cobb, K. M., Westphal, N., Sayani, H. R., Watson, J. T., Di Lorenzo, E., Cheng, H., et al. (2003). Highly variable El Niño-Southern Oscillation throughout the Holocene. *Science*, *424*, 271–276. https://doi.org/10.1126/science.1228246

Collins, M., An, S. Il, Cai, W., Ganachaud, A., Guilyardi, E., Jin, F. F., et al. (2010). The impact of global warming on the tropical Pacific Ocean and El Niño. *Nature Geoscience*, *3*(6), 391–397. https://doi.org/10.1038/ngeo868

Conroy, J. L., Overpeck, J. T., Cole, J. E., Shanahan, T. M., & Steinitz-Kannan, M. (2008). Holocene changes in eastern tropical Pacific climate inferred from a Galápagos lake sediment record. *Quaternary Science Reviews*, *27*(11–12), 1166–1180. https://doi.org/10.1016/j.quascirev.2008.02.015

Corrège, T., Delcroix, T., Récy, J., Beck, W., Cabioch, G., & Le Cornec, F. (2000). Evidence for stronger El Niño-Southern Oscillation (ENSO)events in a mid-Holocene massive coral. *Paleoceanography*, *15*(4), 465–470. https://doi.org/10.1029/1999PA000409

Curry, W. B., Thunell, R. C., & Honjo, S. (1983). Seasonal changes in the isotopic composition of planktonic foraminifera collected in Panama Basin sediment traps. *Earth and Planetary Science Letters*, *64*(1). https://doi.org/10.1016/0012-821X(83)90050-X

De Deckker, P. (2016). The Indo-Pacific Warm Pool: critical to world oceanography and world climate. *Geoscience Letters*, *3*(20), 1–12. https://doi.org/10.1186/s40562-016-0054-3

Dekens, P. S., Lea, D. W., Pak, D. K., & Spero, H. J. (2002). Core top calibration of Mg/Ca in tropical foraminifera: Refining paleotemperature estimation. *Geochemistry, Geophysics, Geosystems*, *3*(4), 1–29. https://doi.org/10.1029/2001GC000200

Dijkstra, H. A. (2006). The ENSO phenomenon: Theory and mechanisms. *Advances in Geosciences*, *6*, 3–15. https://doi.org/10.5194/adgeo-6-3-2006

Elderfield, H., & Ganssen, G. (2000). Past temperature and δ18O of surface ocean waters inferred from foraminiferal Mg/Ca ratios. *Nature*, *405*(6785). https://doi.org/10.1038/35013033

Emile-Geay, J., Cane, M., Seager, R., Kaplan, A., & Almasi, P. (2007). El Niño as a mediator of the solar influence on climate. *Paleoceanography*, *22*(3). https://doi.org/10.1029/2006PA001304

Emile-Geay, J., & Tingley, M. (2016). Inferring climate variability from nonlinear proxies: Application to palaeo-ENSO studies. *Climate of the Past*, *12*(1), 31–50. https://doi.org/10.5194/cp-12-31-2016

Fairbanks, R. G. (1989). A 17,000-year glacio-eustatic sea level record: Influence of glacial melting rates on the Younger Dryas event and deep-ocean circulation. *Nature*. https://doi.org/10.1038/342637a0

Fairbanks, R. G., Sverdlove, M., Free, R., Wiebe, P. H., & Bé, A. W. H. (1982). Vertical distribution and isotopic fractionation of living planktonic foraminifera from the Panama Basin. *Nature*, *298*(5877), 841–844. https://doi.org/10.1038/298841a0

Faul, K. L., Ravelo, A. C., & Delaney, M. L. (2000). Reconstructions of upwelling productivity, and photic zone depth in the eastern equatorial Pacific Ocean using planktonic foraminiferal stable isotopes and abundances. *The Journal of Foraminiferal Research*, *30*(2), 110–125. https://doi.org/10.2113/0300110

Fedorov, A. V., & Philander, S. G. (2001). A stability analysis of tropical ocean-atmosphere interactions: Bridging measurements and theory for El Niño. *Journal of Climate*, *14*(14), 3086–3101. https://doi.org/10.1175/1520-0442(2001)014<3086:ASAOTO>2.0.CO;2

Fiedler, P. C., & Talley, L. D. (2006). Hydrography of the eastern tropical Pacific: A review. *Progress in Oceanography*, *69*(2–4), 143–180. https://doi.org/10.1016/j.pocean.2006.03.008

Ford, H. L., McChesney, C. L., Hertzberg, J. E., & McManus, J. F. (2018). A Deep Eastern Equatorial Pacific Thermocline During the Last Glacial Maximum. *Geophysical Research Letters*, *45*(21), 11806–11816. https://doi.org/10.1029/2018GL079710

Ford, H. L., Ravelo, A. C., & Polissar, P. J. (2015). Reduced El Niño-Southern Oscillation during the last glacial maximum. *Science*, *347*(6219), 255–258. https://doi.org/10.1126/science.1258437

Guilyardi, E., Wittenberg, A., Fedorov, A., Collins, M., Wang, C., Capotondi, A., et al. (2009). Understanding El Niño in ocean-atmosphere general circulation models: Progress and challenges. *Bulletin of the American Meteorological Society*. https://doi.org/10.1175/2008BAMS2387.1

Haines, A., Kovats, R., Campbell-Lendrum, D., & Corvalan, C. (2006). Climate change and human health: impacts, vulnerability, and mitigation. *Lancet*. https://doi.org/10.1016/S0140-6736(06)68933-2

Hemleben, C., W. Allan, O. R. Anderson, and S. Tuntivate (1977), Test morphology, organic layers and chamber formation of the planktonic foraminifer Globorotalia menardii (d'Orbigny), *Journal of Foraminiferal Research*, *7*(1), 1-25.

Hertzberg, J. E., & Schmidt, M. W. (2013). Refining Globigerinoides ruber Mg/Ca paleothermometry in the Atlantic Ocean. *Earth and Planetary Science Letters*, *383*, 123–133. https://doi.org/10.1016/j.epsl.2013.09.044

Hertzberg, J. E., Schmidt, M. W., Bianchi, T. S., Smith, R. K., Shields, M. R., & Marcantonio, F. (2016). Comparison of eastern tropical Pacific TEX86and Globigerinoides ruber Mg/Ca derived sea surface temperatures: Insights from the Holocene and Last Glacial Maximum. *Earth and Planetary Science Letters*, *434*, 320–332. https://doi.org/10.1016/j.epsl.2015.11.050

Hoaglin, D., F. Mosteller, and J. Tukey (1983), *Understanding Robust and Exploratory Data Analysis*, 447 pp., Wiley, New York.

Hönisch, B., Allen, K. A., Lea, D. W., Spero, H. J., Eggins, S. M., Arbuszewski, J., et al. (2013). The influence of salinity on Mg/Ca in planktic foraminifers - Evidence from cultures, core-top sediments and complementary δ18O. *Geochimica et Cosmochimica Acta*, *121*, 196–213. https://doi.org/10.1016/j.gca.2013.07.028

Jacox, M. G., Hazen, E. L., Zaba, K. D., Rudnick, D. L., Edwards, C. A., Moore, A. M., & Bograd, S. J. (2016). Impacts of the 2015–2016 El Niño on the California Current System: Early assessment and comparison to past events. *Geophysical Research Letters*, *46*(13), 7072–7080. https://doi.org/10.1002/2016GL069716

Jin, F. F. (1996). Tropical ocean-atmosphere interaction, the pacific cold tongue, and the El Nino-Southern Oscillation. *Science*, *274*(5284), 76–78. https://doi.org/10.1126/science.274.5284.76

Jin, F. F., Kim, S. T., & Bejarano, L. (2006). A coupled-stability index for ENSO. *Geophysical Research Letters*, *33*(23). https://doi.org/10.1029/2006GL027221

Johnson, G. C., & McPhaden, M. J. (1999). Interior Pycnocline Flow from the Subtropical to the Equatorial Pacific Ocean. *Journal of Physical Oceanography*, *29*(12), 3073–3089. https://doi.org/10.1175/1520-0485(1999)029<3073:ipffts>2.0.co;2

Johnson, G. C., Sloyan, B. M., Kessler, W. S., & McTaggart, K. E. (2002). Direct measurements of upper ocean currents and water properties across the tropical Pacific during the 1990s. *Progress in Oceanography*. https://doi.org/10.1016/S0079-6611(02)00021-6

Kaiser, J., Schefuß, E., Lamy, F., Mohtadi, M., & Hebbeln, D. (2008). Glacial to Holocene changes in sea surface temperature and coastal vegetation in north central Chile: high versus low latitude forcing. *Quaternary Science Reviews*, *27*(21–22), 2064–2075. https://doi.org/10.1016/j.quascirev.2008.08.025

Karnauskas, K. B., Murtugudde, R., & Busalacchi, A. J. (2007). The Effect of the Galápagos Islands on the Equatorial Pacific Cold Tongue. *Journal of Physical Oceanography*, *37*(5), 1266–1281. https://doi.org/10.1175/jpo3048.1

Karnauskas, K. B., Murtugudde, R., & Busalacchi, A. J. (2010). Observing the Galápagos–EUC Interaction: Insights and Challenges. *Journal of Physical Oceanography*, *40*(12), 2768-. https://doi.org/10.1175/2010jpo4461.1

Kessler, W. S. (2006). The circulation of the eastern tropical Pacific: A review. *Progress in Oceanography*, *69*(2–4). https://doi.org/10.1016/j.pocean.2006.03.009

Kessler, W. S. (1990). Observations of long Rossby waves in the northern tropical Pacific. *Journal of Geophysical Research*, *95*(C4), 5183–5217. https://doi.org/10.1029/JC095iC04p05183

Khider, D., Stott, L. D., Emile-Geay, J., Thunell, R., & Hammond, D. E. (2011). Assessing El Niño Southern Oscillation variability during the past millennium. *Paleoceanography*, *26*(3). https://doi.org/10.1029/2011PA002139

Kim, S. T., & Jin, F. F. (2011). An ENSO stability analysis. Part I: Results from a hybrid coupled model. *Climate Dynamics*, *26*(2001), 1593–1607. https://doi.org/10.1007/s00382-010-0796-0

Koutavas, A., deMenocal, P. B., Olive, G. C., & Lynch-Stieglitz, J. (2006). Mid-Holocene El Niño-Southern Oscillation (ENSO) attenuation revealed by individual foraminifera in eastern tropical Pacific sediments. *Geology*, *34*(12), 993–996. https://doi.org/10.1130/G22810A.1

Koutavas, A., & Joanides, S. (2012). El Niño-Southern Oscillation extrema in the Holocene and Last Glacial Maximum. *Paleoceanography*, *27*(4), 1–15. https://doi.org/10.1029/2012PA002378

Koutavas, A., & Lynch-Stieglitz, J. (2004). Variability of the marine ITCZ over the eastern Pacific during the past 30,000 years: Regional perspective and global context. *The Hadley Circulation: Present, Past, and Future*. https://doi.org/10.1007/978-1-4020-2944-8_12

Koutavas, A., Lynch-Stieglitz, J., Marchitto, T. M., & Sachs, J. P. (2002). El Niño-like pattern in ice age tropical Pacific sea surface temperature. *Science*. https://doi.org/10.1126/science.1072376

Lambeck, K., Sambridge, M., Rouby, H., Purcell, A., & Sun, Y. (2014). Sea level and global ice volumes from the Last Glacial Maximum to the Holocene. *Proceedings of the National Academy of Sciences*. https://doi.org/10.1073/pnas.1411762111

Lanzante, J. R. (1996). Resistant, robust and non-parametric techniques for the analysis of climate data: Theory and examples, including applications to historical radiosonde station data. *International Journal of Climatology*, *16*(11), 1197–1226. https://doi.org/10.1002/(SICI)1097-0088(199611)16:11<1197::AID-JOC89>3.0.CO;2-L

Latif, M., & Keenlyside, N. S. (2008). El Nino/Southern Oscillation response to global warming, *106*(49), 20578–20583. https://doi.org/10.1073/pnas.0710860105

Lea, D. W., Mashiotta, T. A., & Spero, H. J. (1999). Controls on magnesium and strontium uptake in planktonic foraminifera determined by live culturing. *Geochimica et Cosmochimica Acta*, *63*(16), 2369-. https://doi.org/10.1016/S0016-7037(99)00197-0

Leduc, G., Vidal, L., Cartapanis, O., & Bard, E. (2009b). Modes of eastern equatorial Pacific thermocline variability: Implications for ENSO dynamics over the last glacial period. *Paleoceanography*, *24*(3), 1–14. https://doi.org/10.1029/2008PA001701

Leduc, G., Vidal, L., Tachikawa, K., Rostek, F., Sonzogni, C., Beaufort, L., & Bard, E. (2007). Moisture transport across Central America as a positive feedback on abrupt climatic changes. *Nature*, *445*(7130), 908–911. https://doi.org/10.1038/nature05578

Locarnini, R., Mishonov, A., Antonov, J., Boyer, T., Garcia, H., Baranova, O., Zweng, M., Paver, M., Reagan, J., and Johnson, D., (2013), World Ocean Atlas 2013, NOAA Atlas NESDIS 73 Vol. 1: Temperature, *NOAA*.

Loubere, P. (2001). Nutrient and oceanographic changes in the Eastern Equatorial Pacific from the last full glacial to the present. *Global and Planetary Change*, *29*(1–2), 77–98. https://doi.org/10.1016/S0921-8181(00)00085-0

Loveley, M. R., Marcantonio, F., Wisler, M. M., Hertzberg, J. E., Schmidt, M. W., & Lyle, M. (2017). Millennial-scale iron fertilization of the eastern equatorial Pacific over the past 100,000 years. *Nature Geoscience*, *10*(10), 760–764. https://doi.org/10.1038/ngeo3024

Liu, Z. (2002). A simple model study of ENSO suppression by external periodic forcing. *Journal of Climate*, *15*(9), 1088–1098. https://doi.org/10.1175/1520-0442(2002)015<1088:ASMSOE>2.0.CO;2

Liu, Z., Kutzbach, J., & Wu, L. (2000). Modeling climate shift of El Nino variability in the Holocene. *Geophysical Research Letters*, *27*(15), 2265–2268. https://doi.org/10.1029/2000GL011452

Liu, Z., Lu, Z., Wen, X., Otto-Bliesner, B. L., Timmermann, A., & Cobb, K. M. (2014). Evolution and forcing mechanisms of El Niño over the past 21,000 years. *Nature*, *515*(7528), 550–553. https://doi.org/10.1038/nature13963

Lu, Z., Liu, Z., & Zhu, J. (2016). Abrupt intensification of ENSO forced by deglacial ice-sheet retreat in CCSM3. *Climate Dynamics*, *46*(5–6), 1877–1891. https://doi.org/10.1007/s00382-015-2681-3

Lu, Z., Liu, Z., Zhu, J., & Cobb, K. M. (2018). A review of paleo El Niño-Southern Oscillation. *Atmosphere*, *9*(4), 1–27. https://doi.org/10.3390/atmos9040130

Lukas, R. (1986). The termination of the Equatorial Undercurrent in the eastern Pacific. *Progress in Oceanography*. https://doi.org/10.1016/0079-6611(86)90007-8

Luo, Y., Lu, J., Liu, F., & Garuba, O. (2017). The role of ocean dynamical thermostat in delaying the El Niño-Like response over the equatorial Pacific to climate warming. *Journal of Climate*, *30*(8), 2811–2827. https://doi.org/10.1175/JCLI-D-16-0454.1

Lynch-Stieglitz, J., Curry, W. B., & Slowey, N. (1999a). A geostrophic transport estimate for the Florida Current from the oxygen isotope composition of benthic foraminifera. *Paleoceanography*, *14*(3), 360–373. https://doi.org/10.1029/1999PA900001

Marchitto, T. M. (2006). Precise multielemental ratios in small foraminiferal samples determined by sector field ICP-MS. *Geochemistry, Geophysics, Geosystems*, *7*(5). https://doi.org/10.1029/2005GC001018

MARGO Project Members. (2009). Constraints on the magnitude and patterns of ocean cooling at the Last Glacial Maximum. *Nature Geoscience*, *2*(2), 127–132. https://doi.org/10.1038/ngeo411

Massey, F. J. (1951). The Kolmogorov-Smirnov Test for Goodness of Fit. *Journal of the American Statistical Association*, *46*(253), 68–78. https://doi.org/10.1080/01621459.1951.10500769

McConnell, M. C., & Thunell, R. C. (2005). Calibration of the planktonic foraminiferal Mg/Ca paleothermometer: Sediment trap results from the Guaymas Basin, Gulf of California. *Paleoceanography*, *20*(2), 1–18. https://doi.org/10.1029/2004PA001077

McGregor, H. V., & Gagan, M. K. (2004). Western Pacific coral δ18O records of anomalous Holocene variability in the El Niño-Southern Oscillation. *Geophysical Research Letters*, *31*(11). https://doi.org/10.1029/2004GL019972

McManus, J. F., Francois, R., Gherardl, J. M., Kelgwin, L., & Drown-Leger, S. (2004). Collapse and rapid resumption of Atlantic meridional circulation linked to deglacial climate changes. *Nature*, *428*(6985), 834–837. https://doi.org/10.1038/nature02494

Meehl, G. A., Teng, H., & Branstator, G. (2006). Future changes of El Niño in two global coupled climate models. *Climate Dynamics*, *26*(6), 549–566. https://doi.org/10.1007/s00382-005-0098-0

Merkel, U., Prange, M., & Schulz, M. (2010). ENSO variability and teleconnections during glacial climates. *Quaternary Science Reviews*. https://doi.org/10.1016/j.quascirev.2009.11.006

Moy, C. M., Seltzer, G. O., Rodbell, D. T., & Anderson, D. M. (2002). Variability of El Niño/Southern Oscillation activity at millennial timescales during the Holocene epoch. *Nature*, *420*(6912), 162–165. https://doi.org/10.1038/nature01194

Nie, X., Gao, S., Wang, F., Chi, J., & Qu, T. (2019). Origins and pathways of the Pacific Equatorial Undercurrent identified by a simulated adjoint tracer. *Journal of Geophysical Research: Oceans*. https://doi.org/10.1029/2018JC014212

Nürnberg, D., Bijma, J., & Hemleben, C. (1996). Assessing the reliability of magnesium in foraminiferal calcite as a proxy for water mass temperatures. *Geochimica et Cosmochimica Acta*, *60*(5), 803–814. https://doi.org/10.1016/0016-7037(95)00446-7

O'Connor, B. M., Fine, R. A., Maillet, K. A., & Olson, D. B. (2002). Formation rates of subtropical underwater in the Pacific Ocean. *Deep-Sea Research Part I: Oceanographic Research Papers*, *49*(9), 1571–1590. https://doi.org/10.1016/S0967-0637(02)00087-0

Otto-Bliesner, B. L., Brady, E. C., Clauzet, G., Tomas, R., Levis, S., & Kothavala, Z. (2006). Last glacial maximum and Holocene climate in CCSM3. *Journal of Climate*, *19*(11), 2526-. https://doi.org/10.1175/JCLI3748.1

Otto-Bliesner, B. L., Brady, E. C., Shin, S. I., Liu, Z., & Shields, C. (2003). Modeling El Niño and its tropical teleconnections during the last glacial-interglacial cycle. *Geophysical Research Letters*, *30*(23). https://doi.org/10.1029/2003GL018553

Patrick, A., & Thunell, R. C. (1997). Tropical Pacific sea surface temperatures and upper water column thermal structure during the last glacial maximum. *Paleoceanography*, *12*(5), 649–657. https://doi.org/10.1029/97PA01553

Pena, L. D., Cacho, I., Ferretti, P., & Hall, M. A. (2008). EI Niño-Southern Oscillation-like variability during glacial terminations and interlatitudinal teleconnections. *Paleoceanography*, *23*(3), 1–8. https://doi.org/10.1029/2008PA001620

Petit, J. R., Jouzel, J., Raynaud, D., Barkov, N. I., Barnola, J. M., Basile, I., et al. (1999). Climate and atmospheric history of the past 420,000 years from the Vostok ice core, Antarctica. *Nature*. https://doi.org/10.1038/20859

Rashid, H. A., Hirst, A. C., & Marsland, S. J. (2016). An atmospheric mechanism for ENSO amplitude changes under an abrupt quadrupling of CO2 concentration in CMIP5 models. *Geophysical Research Letters*, *43*(4), 1687-. https://doi.org/10.1002/2015GL066768

Regenberg, M., Steph, S., Nürnberg, D., Tiedemann, R., & Garbe-Schönberg, D. (2009). Calibrating Mg/Ca ratios of multiple planktonic foraminiferal species with δ18O-calcification temperatures: Paleothermometry for the upper water column. *Earth and Planetary Science Letters*, *278*(3–4), 324–336. https://doi.org/10.1016/j.epsl.2008.12.019

Reimer, P. J., Reimer, R. W., & Blaauw, M. (2013). Calibration of the ^{14}C Record. *Encyclopedia of Quaternary Science: Second Edition*. https://doi.org/10.1016/B978-0-444-53643-3.00045-5

Reimi, M. A., & Marcantonio, F. (2016). Constraints on the magnitude of the deglacial migration of the ITCZ in the Central Equatorial Pacific Ocean. *Earth and Planetary Science Letters*, *453*. https://doi.org/10.1016/j.epsl.2016.07.058

Ritz, S. P., Stocker, T. F., Grimalt, J. O., Menviel, L., & Timmermann, A. (2013). Estimated strength of the Atlantic overturning circulation during the last deglaciation. *Nature Geoscience*, *6*(3). https://doi.org/10.1038/ngeo1723

Rodbell, D. T., Seltzer, G. O., Anderson, D. M., Abbott, M. B., Enfield, D. B., & Newman, J. H. (1999). An ~15,000-year record of El Nino-driven alluviation in Southwestern Ecuador. *Science*, *283*(5401), 516–520. https://doi.org/10.1126/science.283.5401.516

Rongstad, B. L., Marchitto, T. M., & Herguera, J. C. (2017). Understanding the Effects of Dissolution on the Mg/Ca Paleothermometer in Planktic Foraminifera: Evidence from a Novel Individual Foraminifera Method. *Paleoceanography*, *32*(12), 1386–1402. https://doi.org/10.1002/2017PA003179

Rongstad, B. L., Marchitto, T. M., Koutavas, A., Mekik, F., & Ravelo, A. C. (2018). Calibrating a Method for Reconstructing Total and Interannual (ENSO) Variability in the Equatorial Pacific Using Mg/Ca in Individual Planktic Foraminifera. Abstract #434822 presented at 2018 Fall Meeting, American Geophysical Union, Washington, D.C.

Rosenthal, Y., Boyle, E. A., & Slowey, N. (1997). Temperature control on the incorporation of magnesium, strontium, fluorine, and cadmium into benthic foraminiferal shells from Little Bahama Bank: Prospects for thermocline paleoceanography. *Geochimica et Cosmochimica Acta*, *61*(17), 3633–3643. https://doi.org/10.1016/S0016-7037(97)00181-6

Rühlemann, C., Mulitza, S., Müller, P. J., Wefer, G., & Zahn, R. (1999). Warming of the tropical Atlantic Ocean and slowdown of thermohaline circulation during the last deglaciation. *Nature*. https://doi.org/10.1038/990069

Russell, A. D., Hönisch, B., Spero, H. J., & Lea, D. W. (2004). Effects of seawater carbonate ion concentration and temperature on shell U, Mg, and Sr in cultured planktonic foraminifera. *Geochimica et Cosmochimica Acta*, *68*(21), 4347–4361. https://doi.org/10.1016/j.gca.2004.03.013

Rustic, G. T., Koutavas, A., Marchitto, T. M., & Linsley, B. K. (2015). Dynamical excitation of the tropical Pacific Ocean and ENSO variability by Little Ice Age cooling. *Science*, *350*(6267), 1537–1541. https://doi.org/10.1126/science.aac9937

Sadekov, A. Y., Ganeshram, R., Pichevin, L., Berdin, R., McClymont, E., Elderfield, H., & Tudhope, A. W. (2013). Palaeoclimate reconstructions reveal a strong link between El niño-southern oscillation and tropical pacific mean state. *Nature Communications*, *4*, 1–8. https://doi.org/10.1038/ncomms3692

Salau, O. R., Schneider, B., Park, W., Khon, V., & Latif, M. (2012). Modeling the ENSO impact of orbitally induced mean state climate changes. *Journal of Geophysical Research: Oceans*, *11*(5). https://doi.org/10.1029/2011JC007742

Sautter, L. R. (1998), Morphologic and stable isotopic variability within the planktic foraminiferal genus Neogloboquadrina, *Journal of Foraminiferal Research*, *28*(3), 220-232.

Sautter, L. R., & Thunell, R. C. (1991). Seasonal Variability in the δ18O and δ13C of Planktonic Foraminifera from an Upwelling Environment: Sediment Trap Results from the San Pedro Basin, Southern California Bight. *Paleoceanography*, *6*(3), 307–334. https://doi.org/10.1029/91PA00385

Schiebel, R., & Hemleben, C. (2017). *Planktic foraminifers in the modern ocean*. Berlin: Springer. https://doi.org/10.1007/978-3-662-50297-6

Schmidt, M. W., & Lynch-Stieglitz, J. (2011). Florida Straits deglacial temperature and salinity change: Implications for tropical hydrologic cycle variability during the Younger Dryas. *Paleoceanography*, *26*(4). https://doi.org/10.1029/2011PA002157

Schmidt, M. W., Spero, H. J., & Lea, D. W. (2004). Links between salinity variation in the Caribbean and North Atlantic thermohaline circulation. *Nature*, *428*(6979), 160–163. https://doi.org/10.1038/nature02346

Schmidt, M. W., Chang, P., Hertzberg, J. E., Them, T. R., Ji, L., & Otto-Bliesner, B. L. (2012b). Impact of abrupt deglacial climate change on tropical Atlantic subsurface temperatures. *Proceedings of the National Academy of Sciences*, *109*(36), 14348–14352. https://doi.org/10.1073/pnas.1207806109

Schmidt, M. W., Weinlein, W. A., Marcantonio, F., & Lynch-Stieglitz, J. (2012a). Solar forcing of Florida Straits surface salinity during the early Holocene. *Paleoceanography*, *27*(3), 1–12. https://doi.org/10.1029/2012PA002284

Schmitt, A., Elliot, M., Thirumalai, K., La, C., Bassinot, F., Petersen, J., et al. (2019). Single foraminifera Mg/Ca analyses of past glacial-interglacial temperatures derived from G. ruber sensu stricto and sensu lato morphotypes. *Chemical Geology*, *511*, 5. https://doi.org/10.1016/j.chemgeo.2018.11.007

Schneider, T., Bischoff, T., & Haug, G. H. (2014). Migrations and dynamics of the intertropical convergence zone. *Nature*, *513*, 45–53. https://doi.org/10.1038/nature13636

Schrag, D. P., Adkins, J. F., McIntyre, K., Alexander, J. L., Hodell, D. A., Charles, C. D., & McManus, J. F. (2002). The oxygen isotopic composition of seawater during the Last Glacial Maximum. *Quaternary Science Reviews*, *21*(1–3), 331–342. https://doi.org/10.1016/S0277-3791(01)00110-X

Shackleton, N. J. (1987). Oxygen isotopes, ice volume and sea level. *Quaternary Science Reviews*, *6*(3–4), 183–190. https://doi.org/10.1016/0277-3791(87)90003-5

Spero, H. J. (1998). Life History of Stable Isotope Geochemistry of Planktonic Foraminifera. *Department of Geology, University of California*. https://doi.org/10.2147/CIA.S11829

Spero, H. J., Mielke, K. M., Kalve, E. M., Lea, D. W., & Pak, D. K. (2003). Multispecies approach to reconstructing eastern equatorial Pacific thermocline hydrography during the past 360 kyr. *Paleoceanography*, *18*(1). https://doi.org/10.1029/2002PA000814

Stuiver, M., Reimer, P. J., and Reimer R.W (2018). CALIB Radiocarbon Calibration. Executive Version 7.1, http://calib.org.

Them, T. R., Schmidt, M. W., & Lynch-Stieglitz, J. (2015). Millennial-scale tropical atmospheric and Atlantic Ocean circulation change from the Last Glacial Maximum and Marine Isotope Stage 3. *Earth and Planetary Science Letters*, *427*, 47–56. https://doi.org/10.1016/j.epsl.2015.06.062

Thirumalai, K., Partin, J. W., Jackson, C. S., & Quinn, T. M. (2013). Statistical constraints on El Niño Southern Oscillation reconstructions using individual foraminifera: A sensitivity analysis. *Paleoceanography*, *28*(3), 401–412. https://doi.org/10.1002/palo.20037

Thirumalai, K., Quinn, T. M., & Marino, G. (2016). Constraining past seawater δ18O and temperature records developed from foraminiferal geochemistry. *Paleoceanography*, *31*(10), 1409–1422. https://doi.org/10.1002/2016PA002970

Thunell, R. C., & Reynolds, L. A. (1984). Sedimentation of Planktonic Foraminifera: Seasonal Changes in Species Flux in the Panama Basin. *Micropaleontology*, *30*(3), 243–262. https://doi.org/10.2307/1485688

Timmermann, A., Jin, F. F., & Collins, M. (2004). Intensification of the annual cycle in the tropical Pacific due to greenhouse warming. *Geophysical Research Letters*, *31*(12). https://doi.org/10.1029/2004GL019442

Timmermann, A., Lorenz, S. J., An, S. I., Clement, A., & Xie, S. P. (2007b). The effect of orbital forcing on the mean climate and variability of the tropical Pacific. *Journal of Climate*, *20*(16), 4147-. https://doi.org/10.1175/JCLI4240.1

Timmermann, A., Okumura, Y., An, S. I., Clement, A., Dong, B., Guilyardi, E., et al. (2007a). The influence of a weakening of the Atlantic meridional overturning circulation on ENSO. *Journal of Climate*, *20*(19), 4899–4919. https://doi.org/10.1175/JCLI4283.1

Torrence, C., & Compo, G. P. (1998). A Practical Guide to Wavelet Analysis. *Bulletin of the American Meteorological Society*, *79*(1), 61–78. https://doi.org/10.1175/1520-0477(1998)079<0061:APGTWA>2.0.CO;2

Tsuchiya, M., & Talley, L. D. (2004). A Pacific hydrographic section at 88°W: Water-property distribution. *Journal of Geophysical Research: Oceans*, *103*(C6), 12899-. https://doi.org/10.1029/97jc03415

Tudhope, A. W., Chilcott, C. P., Mcculloch, M. T., Cook, E. R., Chappell, J., Ellam, R. M., et al. (2001). Variability in the El Nino-Southern Oscillation Through a Glacial-Interglacial Cycle. *Science*, *291*(5508), 1511–1517. https://doi.org/10.1126/science.1057969

Valley, S., Lynch-Stieglitz, J., & Marchitto, T. M. (2017). Timing of Deglacial AMOC Variability From a High-Resolution Seawater Cadmium Reconstruction. *Paleoceanography*, *32*(11), 1195–1203. https://doi.org/10.1002/2017PA003099

Waliser, D. E., & Gautier, C. (1993). A satellite-derived climatology of the ITCZ. *Journal of Climate*, *6*(11), 2162–2174. https://doi.org/10.1175/1520-0442(1993)006<2162:ASDCOT>2.0.CO;2

Wang, C., & Fiedler, P. C. (2006). ENSO variability and the eastern tropical Pacific: A review. *Progress in Oceanography*, *69*(2–4), 239–266. https://doi.org/10.1016/j.pocean.2006.03.004

White, S. M., Ravelo, A. C., & Polissar, P. J. (2018). Dampened El Niño in the Early and Mid-Holocene due to Insolation-Forced Warming/Deepening of the Thermocline. *Geophysical Research Letters*, *45*(1), 316–326. https://doi.org/10.1002/2017GL075433

Williamson, M. S., Collins, M., Drijfhout, S. S., Kahana, R., Mecking, J. V., & Lenton, T. M. (2018). Effect of AMOC collapse on ENSO in a high-resolution general circulation model. *Climate Dynamics*, *50*(7–8), 2537–25. https://doi.org/10.1007/s00382-017-3756-0

Wit, J. C., Reichart, G. J., A Jung, S. J., & Kroon, D. (2010). Approaches to unravel seasonality in sea surface temperatures using paired single-specimen foraminiferal δ18O and Mg/Ca analyses. *Paleoceanography*, *25*(4). https://doi.org/10.1029/2009PA001857

Woodroffe, C. D., Beech, M. R., & Gagan, M. K. (2003). Mid-late Holocene El Niño variability in the equatorial Pacific from coral microatolls. *Geophysical Research Letters*, *30*(7). https://doi.org/10.1029/2002GL015868

Zheng, W., Braconnot, P., Guilyardi, E., Merkel, U., & Yu, Y. (2008). ENSO at 6ka and 21ka from ocean-atmosphere coupled model simulations. *Climate Dynamics*, *30*(7–8), 745–762. https://doi.org/10.1007/s00382-007-0320-3

Zhu, J., Liu, Z., Brady, E., Otto-Bliesner, B., Zhang, J., Noone, D., et al. (2017). Reduced ENSO variability at the LGM revealed by an isotope-enabled Earth system model. *Geophysical Research Letters*. https://doi.org/10.1002/2017GL073406

FIGURES AND TABLES

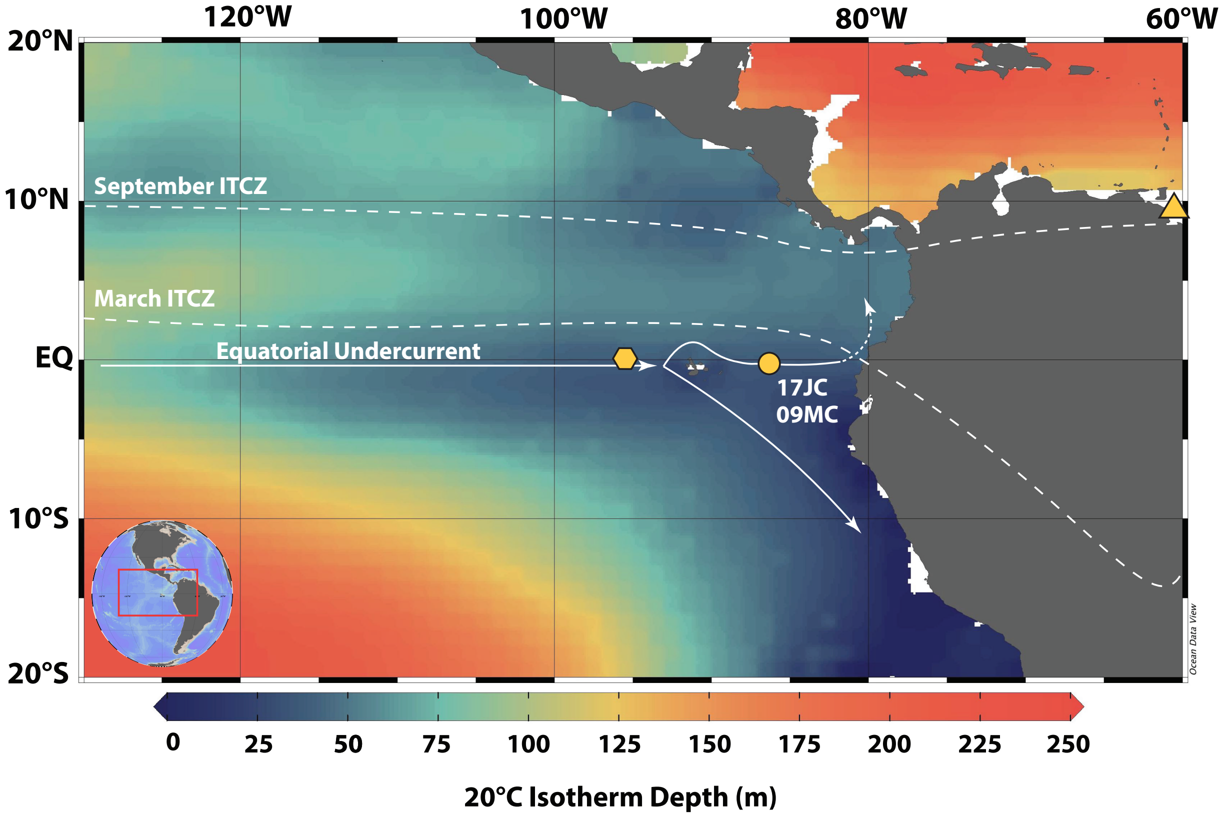
120°W
100°W
80°W
60°W
20°N
10°N
EQ
10°S
20°S
September ITCZ
March ITCZ
Equatorial Undercurrent
17JC
09MC
Ocean Data View
0
25
50
75
100
125
150
175
200
225
250
20°C Isotherm Depth (m)

Figure 1. Regional map of the eastern equatorial Pacific (EEP). Base map displays the depth of the 20°C isotherm, a proxy for thermocline depth (Kessler, 1990). The data that comprise the base map were retrieved from the World Ocean Atlas 2013 dataset (WOA13; Locarnini et al., 2013). Core locations are marked by the yellow circle. The yellow hexagon marks the location of the TAO Array buoy (0°N, 95°W) closest to our core location. The yellow triangle represents the location of the Cariaco Basin. Dashed lines indicate the most northerly and southerly positions of the Intertropical Convergence Zone (ITCZ), and solid arrows indicate the general flow path of the EUC.

Figure 2. Modern hydrographic data illustrating the different modes of surface and subsurface temperature variability within the EEP. (a) A 26-year monthly temperature time series collected at discrete depths from a TAO Array buoy (see Figure 1) correlated against two indices of ENSO: the Southern Oscillation Index (SOI; red) and the Niño 3.4 SST Anomaly (blue). Correlation coefficients are displayed to the right of the temperature data (all significant at the 95% confidence level; correlations with SOI at a one-month lag). Purple curve at 1 m depth represents the annual cycle. The six El Niño events that occurred within the 26-year window are identified using the census list from Golden Gate Weather Services (http://ggweather.com/enso/oni.htm) and highlighted with orange vertical bars. The red box around the data at 40 m marks the dataset used in our sensitivity analysis. (b and c) Seasonal and interannual temperature anomalies of the upper 200 m of the water column at the core location. Anomalies are calculated using the WOA13 annual climatological average from 1955 – 2012 (Locarnini et al., 2013). Casts for Figure 2c were retrieved from the NOAA World Ocean Database Select and Search (https://www.nodc.noaa.gov/OC5/SELECT/dbsearch/dbsearch.html) and chosen based on collection time (during the peak of an ENSO event) and proximity to core location (± 2° lat/lon). Vertical bars close to the y-axis mark the average depth habitat range for *N. dutertrei* at our core location (Loubere, 2001). The gray shaded area in Figure 2c represents the total range of seasonal anomalies (same as plotted in Figure 2b).

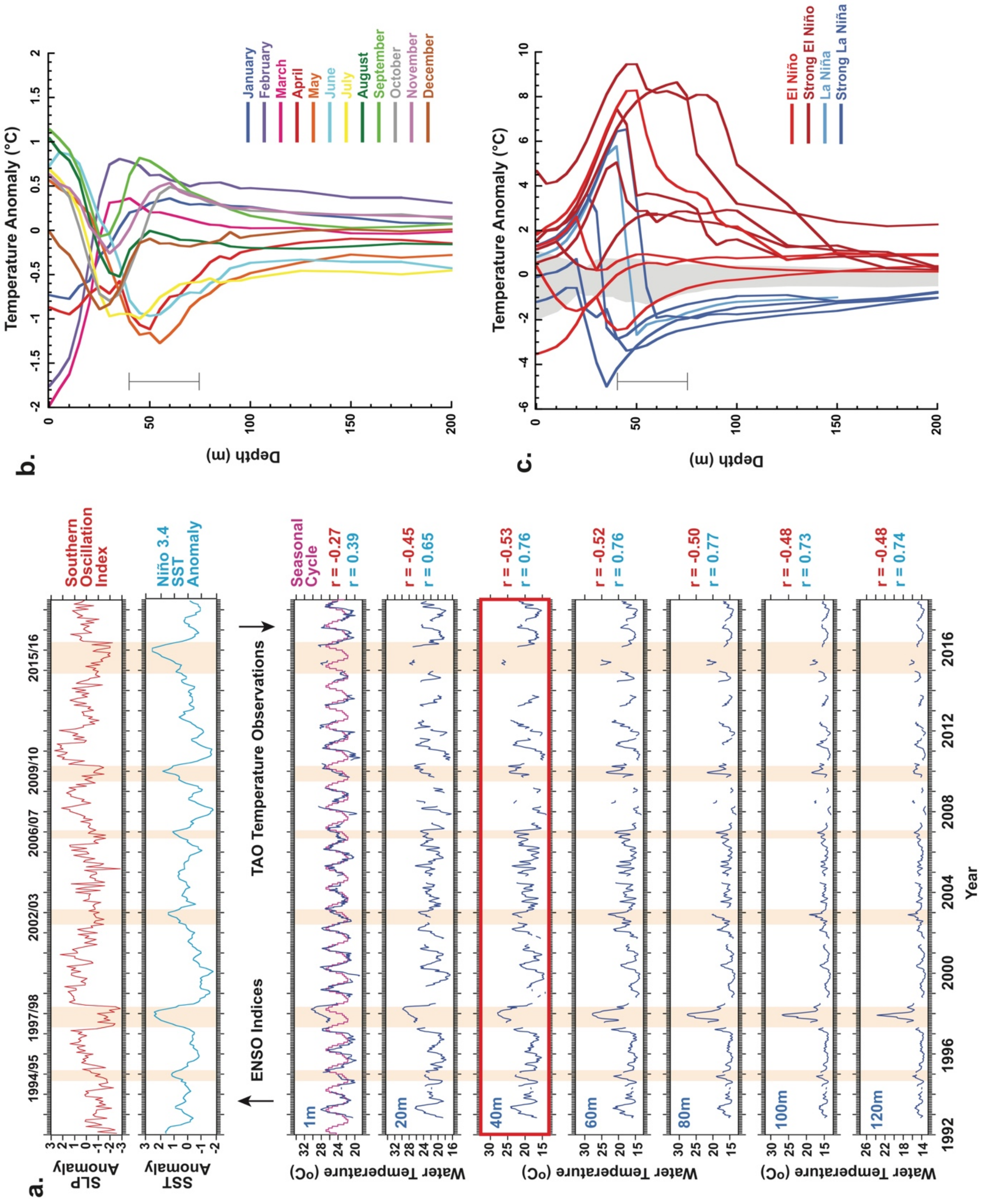
a.
b.
c.
SLP Anomaly
Southern Oscillation Index
SST Anomaly
Niño 3.4 SST Anomaly
ENSO Indices
TAO Temperature Observations
1994/95
1997/98
2002/03
2006/07
2009/10
2015/16
Water Temperature (oC)
Seasonal Cycle
1m
20m
40m
60m
80m
100m
120m
r = -0.27
r = 0.39
r = -0.45
r = 0.65
r = -0.53
r = 0.76
r = -0.52
r = 0.76
r = -0.50
r = 0.77
r = -0.48
r = 0.73
r = -0.48
r = 0.74
Year
1992
1996
2000
2004
2008
2012
2016
Temperature Anomaly (°C)
Depth (m)
January
February
March
April
May
June
July
August
September
October
November
December
El Niño
Strong El Niño
La Niña
Strong La Niña

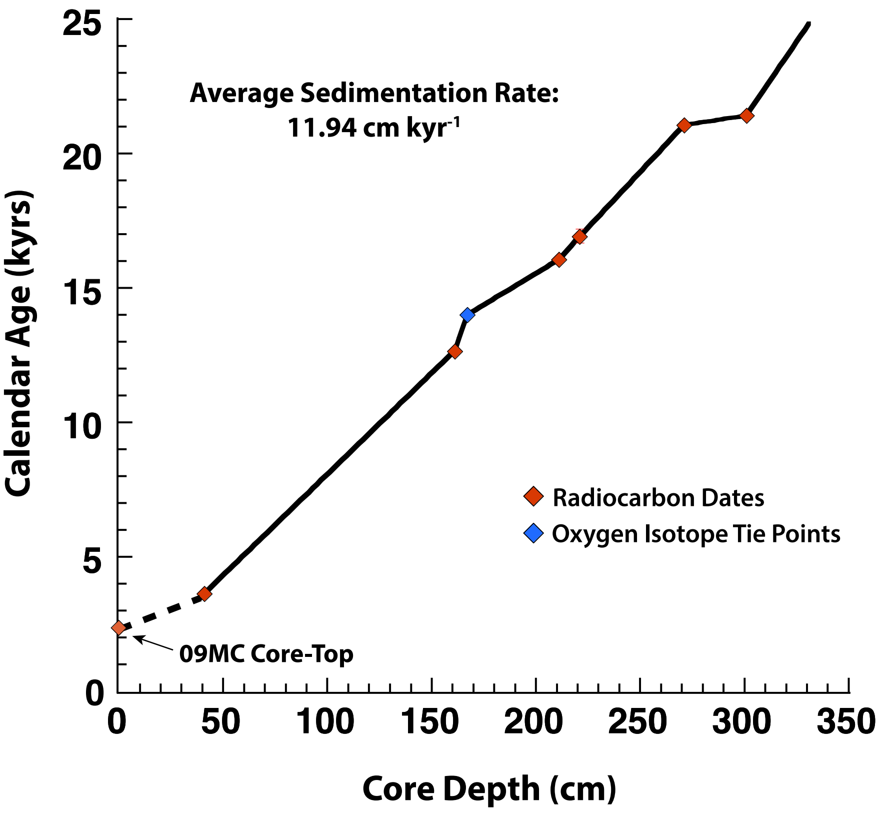

Figure 3. The age model for sediment core 17JC. Red diamonds represent radiocarbon dates and the blue diamond represents a δ^{18}O tie point with NGRIP at the MIS 1 – 2 transition. Red error bars represent the 1σ error on radiocarbon analyses (located behind marker in most cases). The average sedimentation rate (upper left) is based on linear interpolation between radiocarbon dates and the oxygen isotope tie point. 17JC core-top material is assumed to be equal in age to the 09MC core-top (indicated by the black arrow).

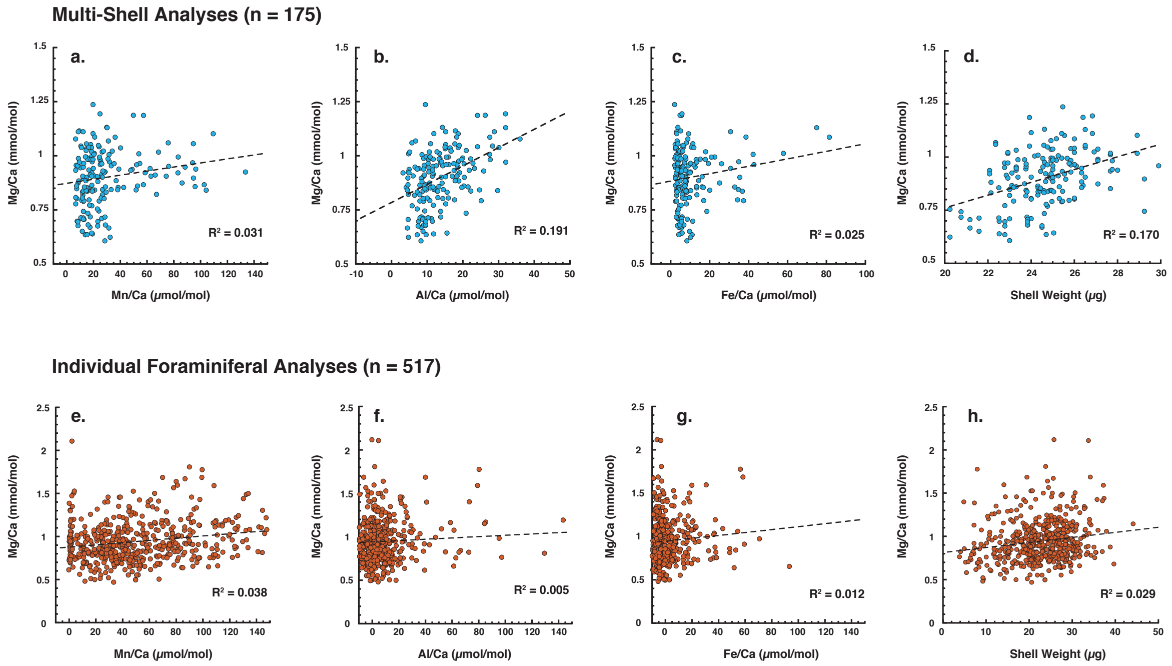

Figure 4. Linear regressions of Mg/Ca against cleaning indicators (Mn/Ca, Al/Ca, and Fe/Ca) and sample size (µg Ca) for our bulk (a – d; blue) and IFA datasets (e – h; red). Coefficients of determination (r^2) are displayed in the bottom right of each subplot.

Table 1

Time Horizons targeted for Individual Foraminiferal Analysis

Time Horizon	Sediment Core	Core Depth (cm)	Age (kyrs)	# Picked Individuals	Mean (°C)	BSD (°C)
Modern/Late Holocene (Mod/LH)	09MC	0 – 0.5	2.20	82	19.5	2.95
Mid-Holocene (MH)	17JC	84 – 85	6.90	78	18.1	2.74
Early Holocene (EH)	17JC	112 – 113	9.01	71	20.2	2.80
Younger Dryas (YD)	17JC	152 – 153	12.0	71	19.0	2.73
Bølling-Allerød (BA)	17JC	164 – 165	13.4	69	18.4	2.86
Heinrich Stadial 1 (HS1)	17JC	196 – 197	15.9	72	18.4	2.80
Last Glacial Maximum (LGM)	17JC	260 – 261	20.2	74	16.2	2.81

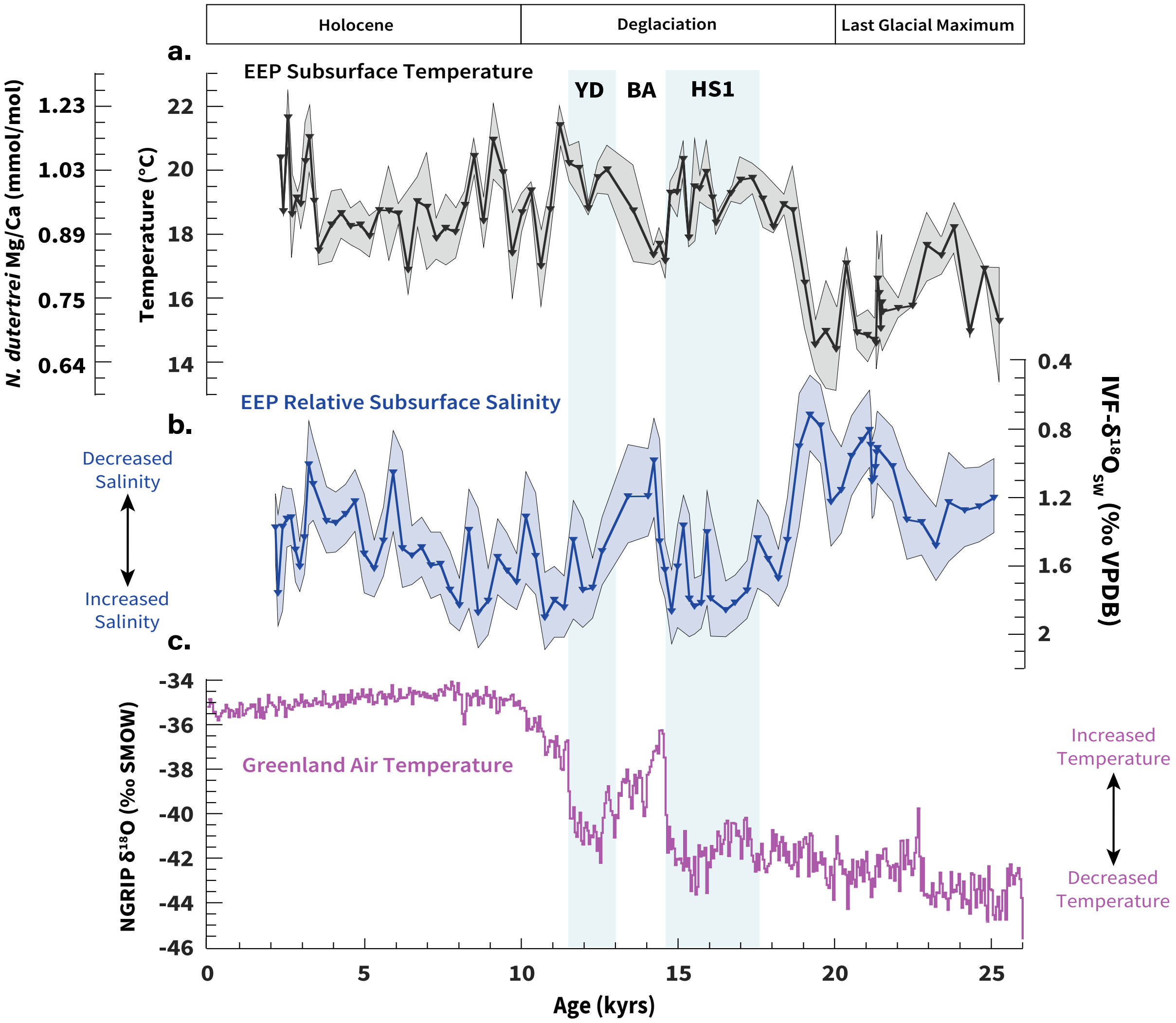

Figure 5. Down-core records of (a) Mg/Ca-derived subsurface temperature and (b) IVF-$\delta^{18}O_{SW}$ compared against (c) the NGRIP $\delta^{18}O$ ice core record of Greenland air temperature. Note the double y-axis in the top panel which shows the equivalent Mg/Ca value for each calculated subsurface temperature. Gray error envelopes on the temperature record represent 1σ on replicated measurements. Light blue error envelope on the IVF-$\delta^{18}O_{SW}$ record represents the compounded 1σ error calculated using PSU Solver (Thirumalai et al., 2016). Stadial events during the last deglaciation (the YD and HS1) are highlighted in blue.

Table 2

Monte Carlo Average BSDs and Associated Confidence Limits

Modeled ENSO Scenario	Monte Carlo Average BSD (°C)	Lower 95% CI (°C)	Upper 95% CI (°C)	“True” BSD* (°C)	% Difference
100% Dampened	1.961	1.814	2.113	1.969	0.41
90% Dampened	1.998	1.853	2.147	2.001	0.15
80% Dampened	2.044	1.894	2.198	2.055	0.54
70% Dampened	2.105	1.950	2.264	2.113	0.38
60% Dampened	2.166	2.002	2.334	2.183	0.87
50% Dampened	2.239	2.069	2.414	2.254	0.67
40% Dampened	2.321	2.139	2.509	2.340	0.82
30% Dampened	2.405	2.205	2.610	2.424	0.79
20% Dampened	2.499	2.285	2.721	2.513	0.56
10% Dampened	2.590	2.362	2.826	2.610	0.77
Non-adjusted	2.690	2.444	2.943	2.715	0.93
10% Amplified	2.797	2.534	3.068	2.819	0.78
20% Amplified	2.906	2.628	3.193	2.927	0.72
30% Amplified	3.013	2.713	3.321	3.038	0.83
40% Amplified	3.123	2.809	3.447	3.149	0.83
50% Amplified	3.240	2.905	3.586	3.267	0.83
60% Amplified	3.354	3.008	3.711	3.387	0.98
70% Amplified	3.472	3.102	3.853	3.507	1.00
80% Amplified	3.603	3.212	4.006	3.628	0.69
90% Amplified	3.726	3.322	4.142	3.749	0.61
100% Amplified	3.844	3.424	4.276	3.877	0.85

**The “true” BSD refers to the calculated BSD of the entire altered temperature time series.*

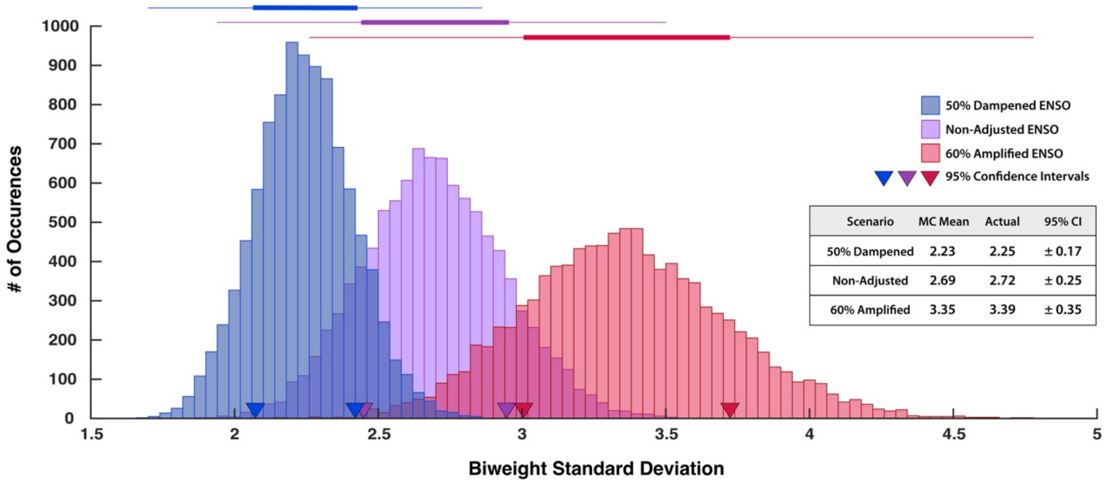

Scenario	MC Mean	Actual	95% CI
50% Dampened	2.23	2.25	± 0.17
Non-Adjusted	2.69	2.72	± 0.25
60% Amplified	3.35	3.39	± 0.35

Figure 6. Comparison of BSD uncertainty estimates from the 50% dampened ENSO scenario (blue) and the 60% amplified ENSO scenario (red) against the non-adjusted ENSO scenario (purple). Each histogram is comprised of the 10,000 calculated BSDs from each Monte Carlo resampling of their respective temperature time series. Inverted triangles along the x-axis mark the 95% confidence limits of their respective histograms. The lines above the histograms represent the total range of calculated BSDS (thin line) and 95% confidence limits (thick lines) of each scenario. The differences between the mean of the Monte Carlo BSDs ("MC mean") and the true BSD of each scenario's respective time series ("Actual") are summarized in the inset table to the right.

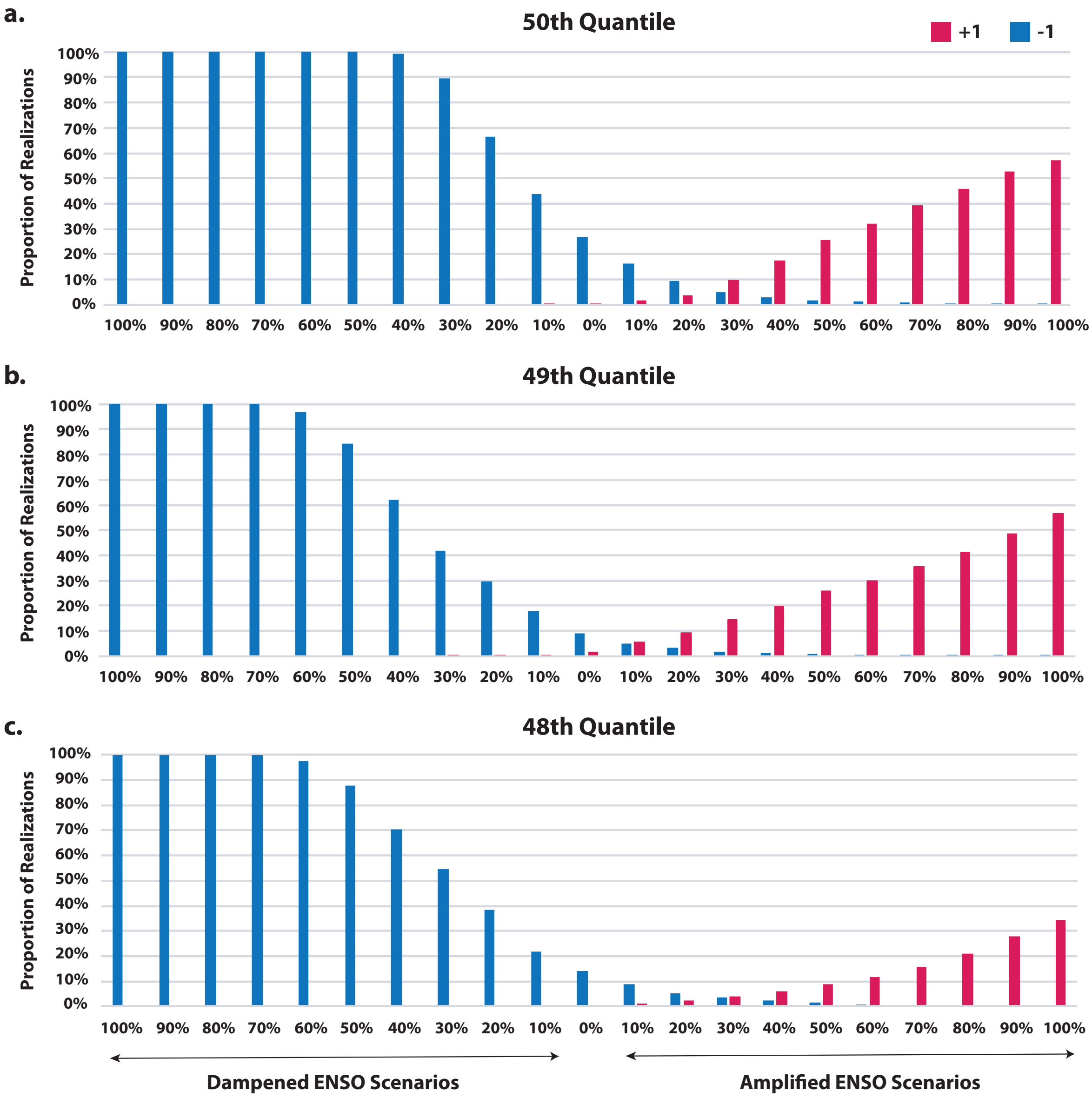

Figure 7. Bar graphs summarizing the sensitivity of the warmest three quantiles to prescribed changes in the amplitude of ENSO (50th, 49th, and 48th quantiles in the top, middle, and bottom panels, respectively). Bars represent the proportion of the 10,000 Monte Carlo datasets that produced a significantly reduced (-1; blue) or enhanced (+1; red) result. The 21 ENSO scenarios are arranged along the x-axis, beginning with the 100% dampened ENSO scenario to the far left and ending with the 100% amplified scenario on the far right; the non-adjusted (0%) ENSO scenario is centered on the axis.

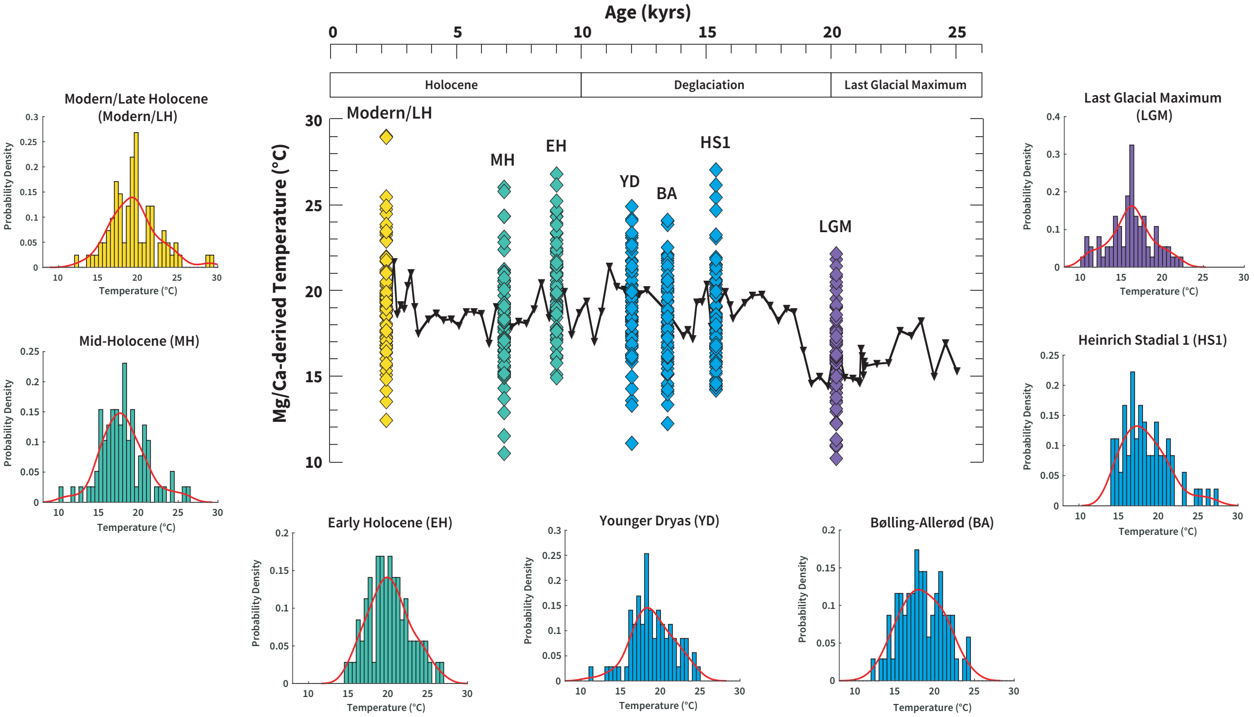

Figure 8. IFA data and related distributions from seven discrete time slices spanning the last 25 kyrs. Colored diamonds in the central figure represent temperature estimates from individual foraminifera (see Table 1 for sample sizes of each time slice). Colors are assigned accordingly: yellow (Modern/LH), green (Holocene), blue (deglaciation), and purple (LGM). The down-core subsurface temperature record (black line with black diamonds) is shown for reference. Labels and colors for each IFA population correspond to colored histograms surrounding the central figure. Histograms move from youngest to oldest from right (beginning with the yellow Modern/LH distribution) to left (ending with the purple LGM distribution). Probability density functions (red lines on histograms) are generated from their constituent IFA datasets to better visualize the shape of each IFA distribution.

Table 3

Results from the two-sample Kolmogorov-Smirnov Goodness-of-Fit Tests[a]

Time Slice	Mod/LH	MH	EH	YD	BA	HS1	LGM
Modern/Late Holocene	x	-	-	-	-	-	-
Mid-Holocene	**0.003**	x	-	-	-	-	-
Early Holocene	0.123	**<0.001**	x	-	-	-	-
Younger-Dryas	0.503	0.100	**0.028**	x	-	-	-
Bølling-Allerød	0.112	0.489	**0.002**	0.471	x	-	-
Heinrich Stadial 1	**0.024**	0.975	**<0.001**	0.190	0.959	x	-
Last Glacial Maximum	**<0.001**	**<0.001**	**<0.001**	**<0.001**	**<0.001**	**<0.001**	x

[a] *P-values in bold are significant at the 95% confidence level (a = 0.05).*

Table 4

Results from the Brown-Forsythe Tests for Homogeneity of Variance[b]

Time Slice	Mod/LH	MH	EH	YD	BA	HS1	LGM
Modern/Late Holocene	x	-	-	-	-	-	-
Mid-Holocene	0.71	x	-	-	-	-	-
Early Holocene	0.59	0.86	x	-	-	-	-
Younger-Dryas	0.55	0.81	0.94	x	-	-	-
Bølling-Allerød	0.85	0.84	0.69	0.65	x	-	-
Heinrich Stadial 1	0.90	0.81	0.67	0.63	0.95	x	-
Last Glacial Maximum	0.44	0.68	0.80	0.85	0.52	0.51	x

[b] *P-values in bold are significant at the 95% confidence level (a = 0.05).*

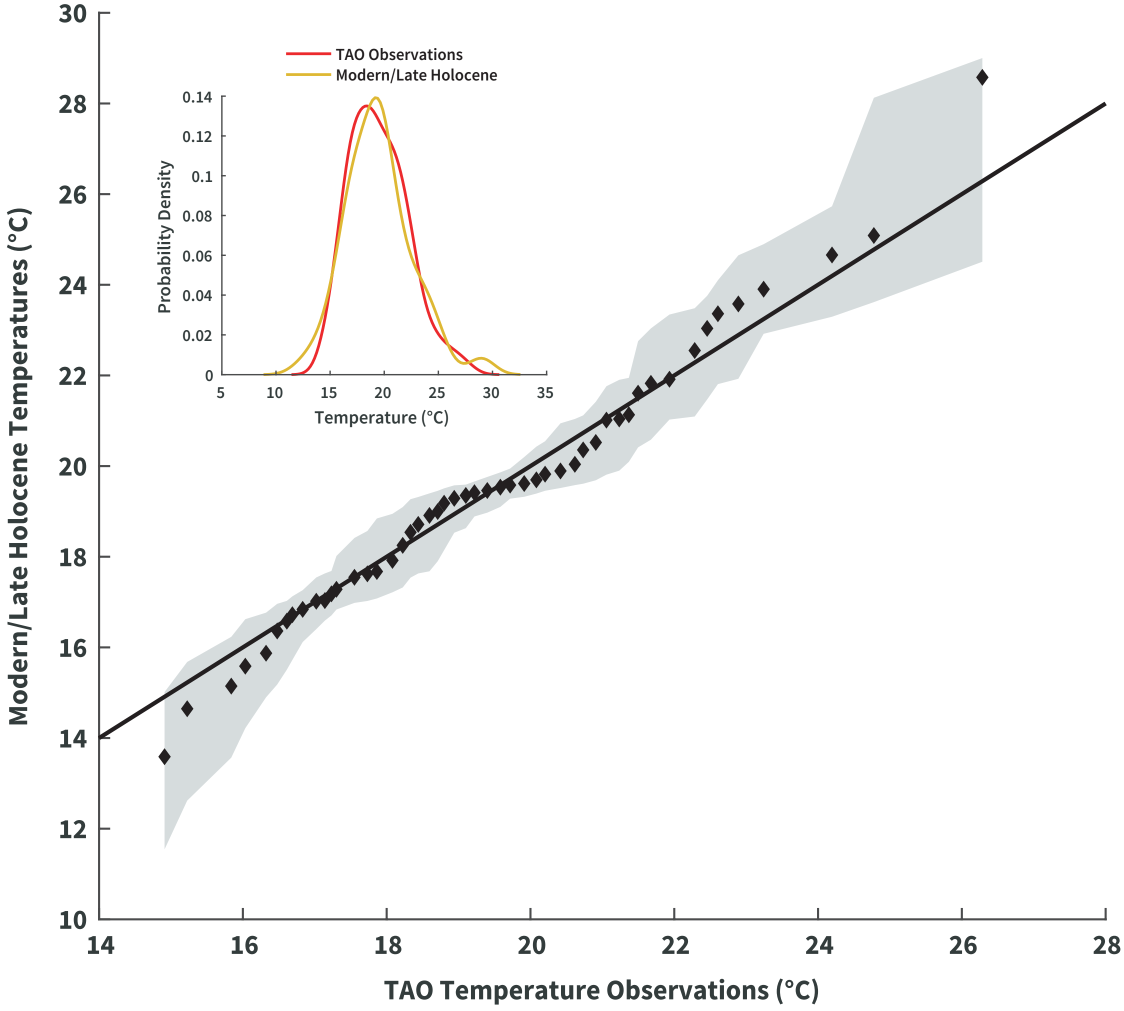

Figure 9. Q-Q plot comparing the quantiles of the TAO temperature observations at 40 m against the quantiles from the Modern/LH population of individual foraminifera from the 09MC core-top. Gray envelope represents 90% confidence limits derived through a Monte Carlo resampling approach (Ford et al., 2015). Solid black line represents the 1:1 line. The inset figure compares the probability density functions of the TAO observations (red line) with the Modern/LH population (yellow line).

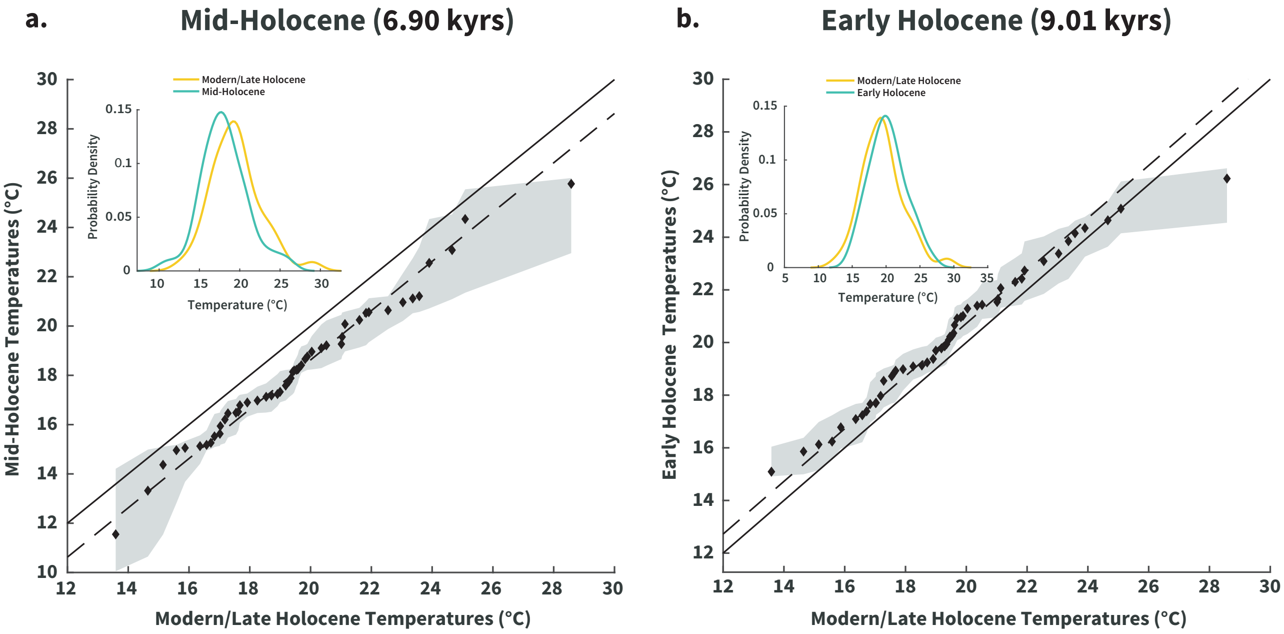

Figure 10. Q-Q plots comparing the quantiles of the (a) MH and (b) EH time slices against the Modern/LH IFA population from the 09MC core-top. The solid black lines represent the 1:1 line, and the dashed black lines represent the mean-adjusted 1:1 line. Gray envelope represents 90% confidence limits derived through a Monte Carlo resampling approach (Ford et al., 2015). Inset figures compare the probability density functions of the Modern/LH population (yellow line) with the down-core Holocene time slices (green lines).

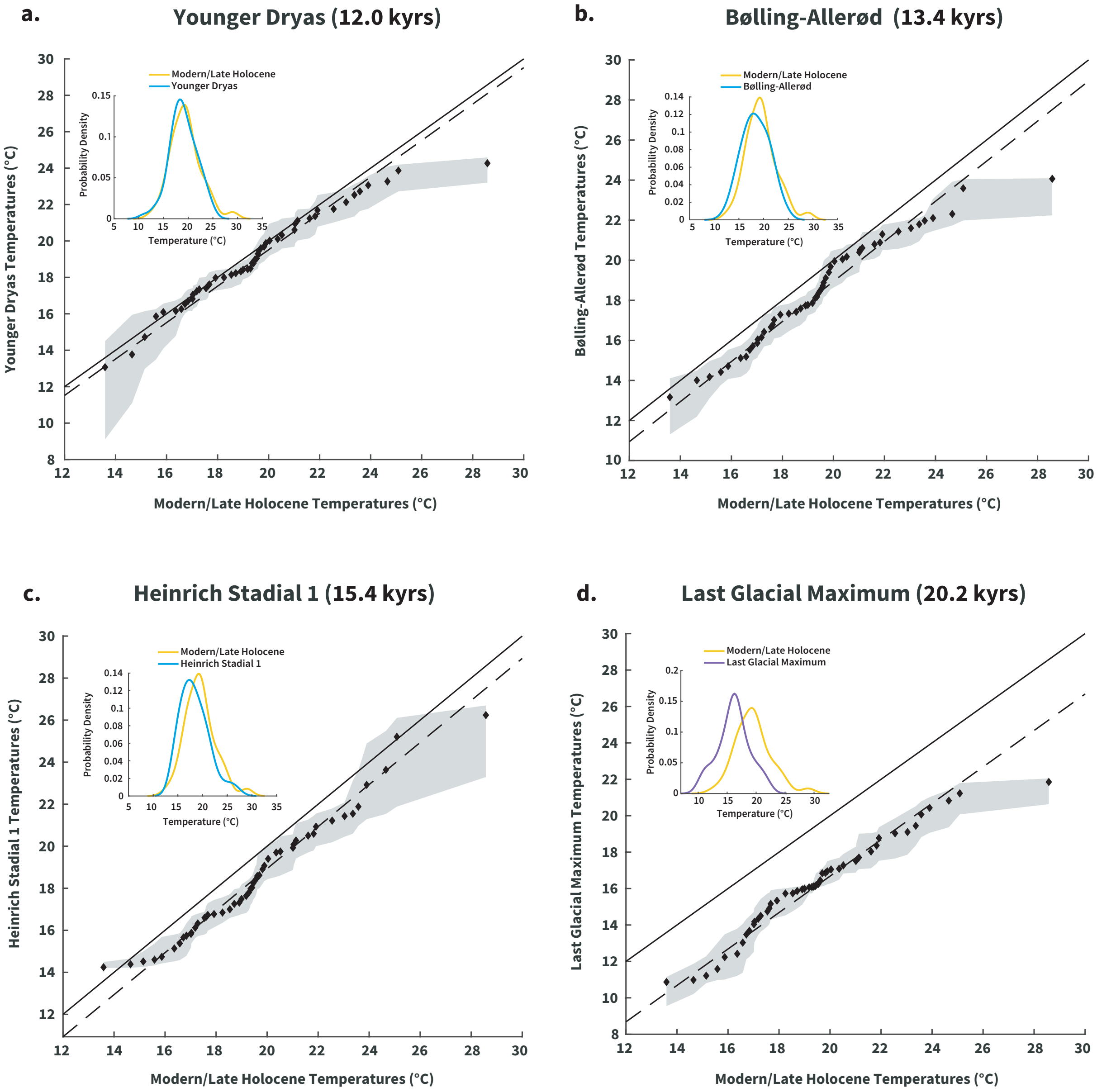

Figure 11. Same as figure 10 but comparing the quantiles of (from top left to bottom right) the YD, BA, HS1 and LGM time slices against the quantiles of the Modern/LH IFA population. Inset figures compare the IFA probability density functions of the Modern/LH population (yellow line) with the 17JC deglacial (blue lines) and glacial time slices (purple line).

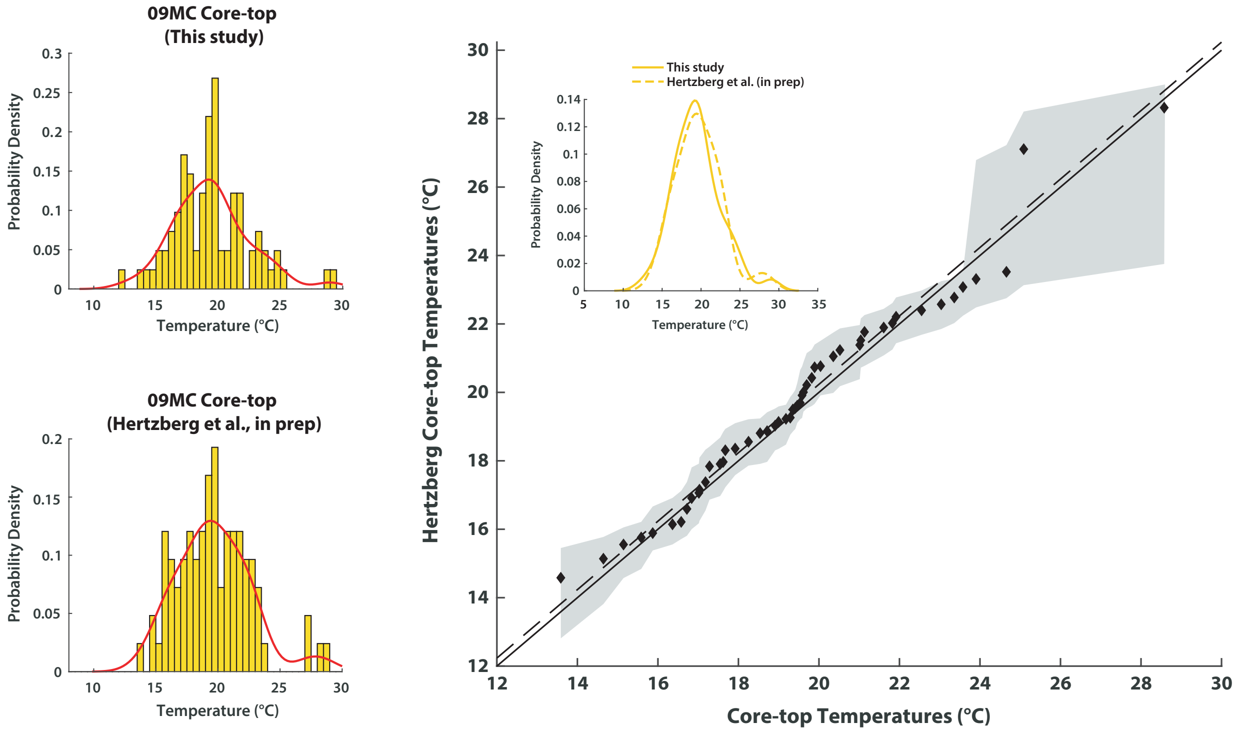

Figure 12. Comparison of two independently generated paleotemperature distributions from the core-top of 09MC. The solid black lines represent the 1:1 line, and the dashed black lines represent the mean-adjusted 1:1 line. Gray envelope represents 90% confidence limits derived through a Monte Carlo resampling approach (Ford et al., 2015). Inset figures compare the probability density functions of the Modern/LH time slice (this study; solid yellow line) with the second 09MC population (Hertzberg et al., in prep; dashed yellow line).

Figure 13. A synthesis of geochemical proxy records illustrating tropical Pacific mean state change over the last 25 kyrs. (a) IFA time slices from cores 17JC and 09MC normalized to their respective means. Labels for time slices are presented within the gray bar. (b) Solar insolation curves: March minus September insolation (Mar – Sept) at the equator (orange line) and austral winter insolation (JJA) at 30°S (purple line). (c) Compilation of EEP subsurface temperature records: 17JC (this study; black line), ODP site 1240 (Pena et al., 2008; red line), and CD38-17 (Sadekov et al., 2013; yellow line). Paleotemperatures from both site 1240 and CD38-17 were recalculated using Dekens et al. (2002) *N. dutertrei* equation with depth-correction term. Since the samples by Sadekov et al. (2013) were not subjected to the reductive step during sample cleaning, a 10% reduction in Mg/Ca was applied throughout the CD38-17 record. (d) Zonal SST gradient calculation performed by Koutavas and Joanides (2012) (refer to original publication for compilation of records included in computation). (e) Record of sediment reflectance in the green spectrum from ODP site 1002 in the Cariaco Basin north of Venezuela. Record reflects qualitative shifts in the latitudinal position of the ITCZ (green scale bar). (f) Record or atmospheric CO_2 concentrations from multiple ice cores recovered from Antarctica (Bereiter et al., 2015). Cores include: Law Dome (green and yellow circles), Dome C (blue circles), WAIS (orange circles), and Siple Dome (red circles) (refer to Bereiter et al., 2015 for sources to original data).

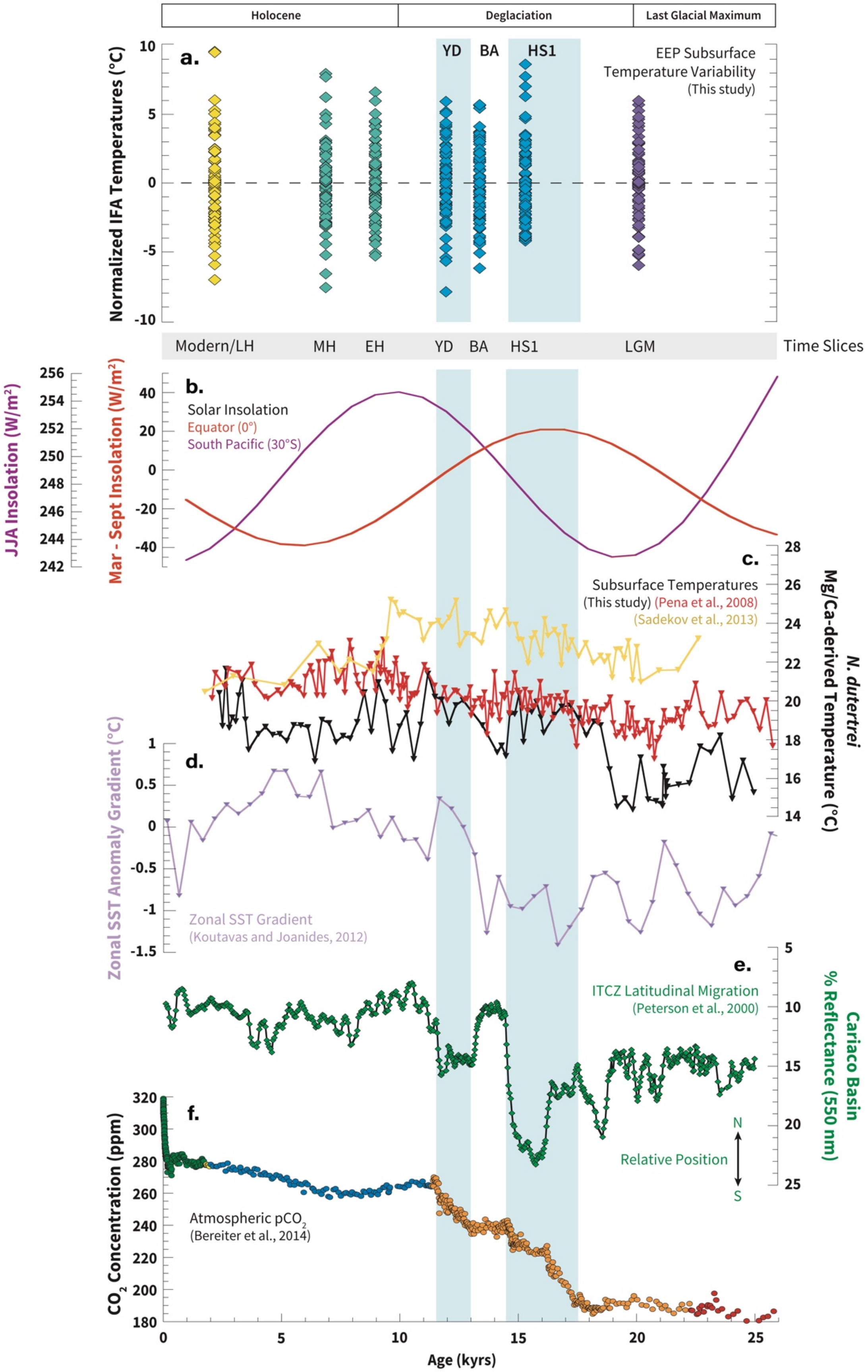
Holocene
Deglaciation
Last Glacial Maximum
a.
YD
BA
HS1
EEP Subsurface
Temperature Variability
(This study)
Normalized IFA Temperatures (°C)
10
5
0
-5
-10
Modern/LH
MH
EH
YD
BA
HS1
LGM
Time Slices
b.
Solar Insolation
Equator (0°)
South Pacific (30°S)
JJA Insolation (W/m²)
256
254
252
250
248
246
244
242
Mar - Sept Insolation (W/m²)
40
20
0
-20
-40
c.
Subsurface Temperatures
(This study) (Pena et al., 2008)
(Sadekov et al., 2013)
N. dutertrei
Mg/Ca-derived Temperature (°C)
28
26
24
22
20
18
16
14
d.
Zonal SST Anomaly Gradient (°C)
1
0.5
0
-0.5
-1
-1.5
Zonal SST Gradient
(Koutavas and Joanides, 2012)
e.
ITCZ Latitudinal Migration
(Peterson et al., 2000)
Cariaco Basin
% Reflectance (550 nm)
5
10
15
20
25
N
Relative Position
S
f.
CO2 Concentration (ppm)
320
300
280
260
240
220
200
180
Atmospheric pCO2
(Bereiter et al., 2014)
0
5
10
15
20
25
Age (kyrs)

VITA

RYAN H. GLAUBKE
Dept. Ocean, Earth and Atmospheric Sciences
Old Dominion University
Norfolk, VA 23529
Phone: 757.513.8068
email: rglau001@odu.edu

EDUCATION

Present	**M.Sc. Ocean and Earth Sciences** Old Dominion University, Norfolk, VA Thesis: *The evolution of the El Niño-Southern Oscillation and tropical Pacific climate across the last deglaciation* Advisor: Dr. Matthew W. Schmidt
2016	**B.Sc. Ocean and Earth Sciences, *cum laude*** Old Dominion University, Norfolk, VA Capstone Research: *Benthic oxygen and nutrient dynamics in the Lafayette River: assessment of spatial and temporal variations in sediment oxygen demand*

PROFESSIONAL EXPERIENCE

Present	**Graduate Research Assistant**, Schmidt Paleoceanography and Paleoclimatology Laboratory
2016 – 2019	**Teaching Assistant**, Old Dominion University
Spring 2016	**Undergraduate Research Assistant** – Schmidt Paleoceanography and Paleoclimatology Laboratory
2015 – 2016	**Undergraduate Capstone Research** – OEAS Field Studies Laboratory (Old Dominion University)
2014 – 2015	**Undergraduate Research Assistant** – Darby Arctic Paleoclimate Laboratory (Old Dominion University)

SELECT CONFERENCE PROCEEDINGS (most recent first)

(1) **Glaubke, R. H.,** M. W. Schmidt, J. E. Hertzberg, L. G. Ward, and F. Marcantonio. Millennial-Scale Variations in ENSO Activity across the Last Deglaciation: Insights from Individual Foraminiferal Analysis. 13th International Conference on Paleoceanography, Sydney, Australia, 2019 (*accepted*).

(2) **Glaubke, R. H.,** M. W. Schmidt, J. E. Hertzberg, L. Warner, F. Marcantonio, and T. S. Bianchi. Utilizing Individual Foraminiferal Analysis to investigate the history of the El Niño – Southern Oscillation. 2018 International Symposium on Foraminifera, Edinburgh, Scotland, UK, 2018.

(3) **Glaubke, R. H.,** M. W. Schmidt, L. Warner, J. E. Hertzberg, F. Marcantonio, and T. S. Bianchi. Changes in Eastern Equatorial Pacific Thermocline Structure across the Last Deglaciation: Evidence from the Carnegie Ridge. AGU Fall Meeting, New Orleans, LA, 2017.

(4) **Glaubke, R. H.** and M. W. Schmidt. Tropical North Atlantic Subsurface Temperatures: A Proxy for AMOC Variability. AGU Fall Meeting, San Francisco, CA, 2016.